Neuron

Article

Piezo1-Mediated Ca^{2+} Activities Regulate Brain Vascular Pathfinding during Development

Graphical Abstract

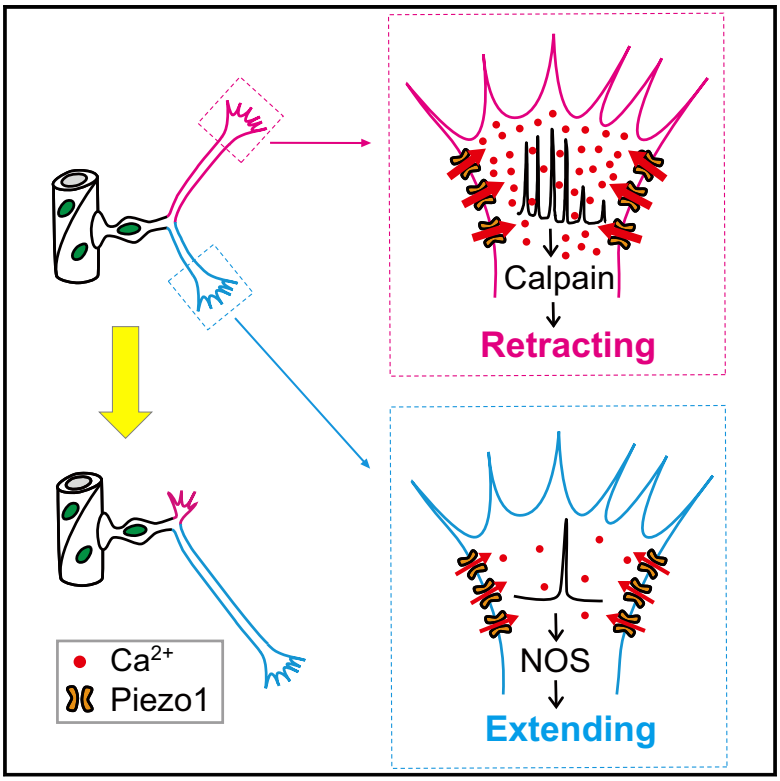

Authors

Ting-ting Liu, Xu-fei Du, Bai-bing Zhang, ..., Shan-ye Gu, Qi Chen, Jiu-lin Du

Correspondence

forestdu@ion.ac.cn

In Brief

Endothelial tip cell (ETC) pathfinding is crucial for vascular patterning. Liu et al. report that Piezo1-mediated local Ca^{2+} activities at primary branches of ETCs regulate branch dynamics to accomplish ETC pathfinding during zebrafish brain vascular development, leading to proper patterning of the brain vasculature.

Highlights

- Brain endothelial tip cells (ETCs) show local Ca^{2+} transients at primary branches
- High- and low-frequency Ca^{2+} transients distinctly regulate ETC branch dynamics
- Mechanosensitive Piezo1 channels mediate local Ca^{2+} transients of ETC branches
- Mutating *piezo1* impairs ETC pathfinding and brain vascular patterning

Liu et al., 2020, Neuron *108*, 180–192
October 14, 2020
https://doi.org/10.1016/j.neuron.2020.07.025

CellPress

CellPress

Neuron

Article

Piezo1-Mediated Ca^{2+} Activities Regulate Brain Vascular Pathfinding during Development

Ting-ting Liu,[1,2] Xu-fei Du,[1] Bai-bing Zhang,[1] Hua-xing Zi,[1,2] Yong Yan,[1,3] Jiang-an Yin,[1] Han Hou,[1] Shan-ye Gu,[1] Qi Chen,[1] and Jiu-lin Du[1,2,3,4,*]

[1]Institute of Neuroscience, State Key Laboratory of Neuroscience, Center for Excellence in Brain Science and Intelligence Technology, Shanghai Research Center for Brain Science and Brain-Inspired Intelligence, Chinese Academy of Sciences, 320 Yue-Yang Road, Shanghai 200031, China

[2]University of Chinese Academy of Sciences, 19A Yu-Quan Road, Beijing 100049, China

[3]School of Life Science and Technology, ShanghaiTech University, 319 Yue-Yang Road, Shanghai 200031, China

[4]Lead Contact

*Correspondence: forestdu@ion.ac.cn

https://doi.org/10.1016/j.neuron.2020.07.025

SUMMARY

During development, endothelial tip cells (ETCs) located at the leading edge of growing vascular plexus guide angiogenic sprouts to target vessels, and thus, ETC pathfinding is fundamental for vascular pattern formation in organs, including the brain. However, mechanisms of ETC pathfinding remain largely unknown. Here, we report that Piezo1-mediated Ca^{2+} activities at primary branches of ETCs regulate branch dynamics to accomplish ETC pathfinding during zebrafish brain vascular development. ETC branches display spontaneous local Ca^{2+} transients, and high- and low-frequency Ca^{2+} transients cause branch retraction through calpain and branch extension through nitric oxide synthase, respectively. These Ca^{2+} transients are mainly mediated by Ca^{2+}-permeable Piezo1 channels, which can be activated by mechanical force, and mutating *piezo1* largely impairs ETC pathfinding and brain vascular patterning. These findings reveal that Piezo1 and downstream Ca^{2+} signaling act as molecular bases for ETC pathfinding and highlight a novel function of Piezo1 and Ca^{2+} in vascular development.

INTRODUCTION

The blood vasculature in the brain is a hierarchically ramified vessel network with a total vessel length of a few hundred miles in the human and tailored for efficiently delivering the blood to each brain area (Padget, 1956; Tam and Watts, 2010; Zlokovic, 2008). How such a highly sophisticated but well-organized vessel network is constructed has long been fascinating biologists (Andreone et al., 2015; Chen et al., 2012; Tam and Watts, 2010; Wälchli et al., 2015; Zlokovic, 2008). It is known that the formation of the brain vasculature is initiated by vessel invasion from the surrounding peri-neural vascular plexus around the ventral neural tube during early development and then the brain vasculature is expanded by continuous emergence and growth of newborn vessels from pre-existing ones, a process known as angiogenesis (Andreone et al., 2015; Tam and Watts, 2010; Wälchli et al., 2015).

During the expansion process, path selection of growing vessels determines the three-dimensional pattern of the brain vasculature. Previous studies mainly focus on the molecular mechanism of brain angiogenesis and have identified a number of important molecules, including the vascular endothelial growth factor (VEGF), Wnt, integrins, GPR124, NogoA, and microRNA-132, which are involved in regulation of vessel invasion, angiogenic sprouting capacity, proliferation and migration of endothelial cells (ECs), or vascular integrity (Andreone et al., 2015; Eichmann et al., 2005; Gerhardt et al., 2004; James et al., 2009; Kuhnert et al., 2010; Stenman et al., 2008; Tam and Watts, 2010; Wälchli et al., 2013, 2015; Xu et al., 2017; Zhu et al., 2002). However, it is still poorly understood how growing vessels make appropriate path selection to form proper patterning. This is mainly due to technical challenge in visualizing the entire process of vessel growth in the intact brain.

At the forefront of growing vessels, there is a vascular endothelial tip cell (ETC) that usually extends a few motile primary branches and many dynamical fine filopodia (Adams and Alitalo, 2007; Geudens and Gerhardt, 2011; Wälchli et al., 2015). ETCs navigate through tissue microenvironments and steer angiogenic sprouts to their appropriate targets, a process known as pathfinding (Eichmann et al., 2005; Fischer et al., 2019). Although ETC pathfinding is believed to be critical for the proper patterning of the vasculature in the brain as well as in all other organs, its underlying mechanism remains elusive (Eichmann et al., 2005; Fischer et al., 2019).

It is known that Ca^{2+} plays important roles in a broad range of biological processes (Berridge et al., 2000), such as neuronal

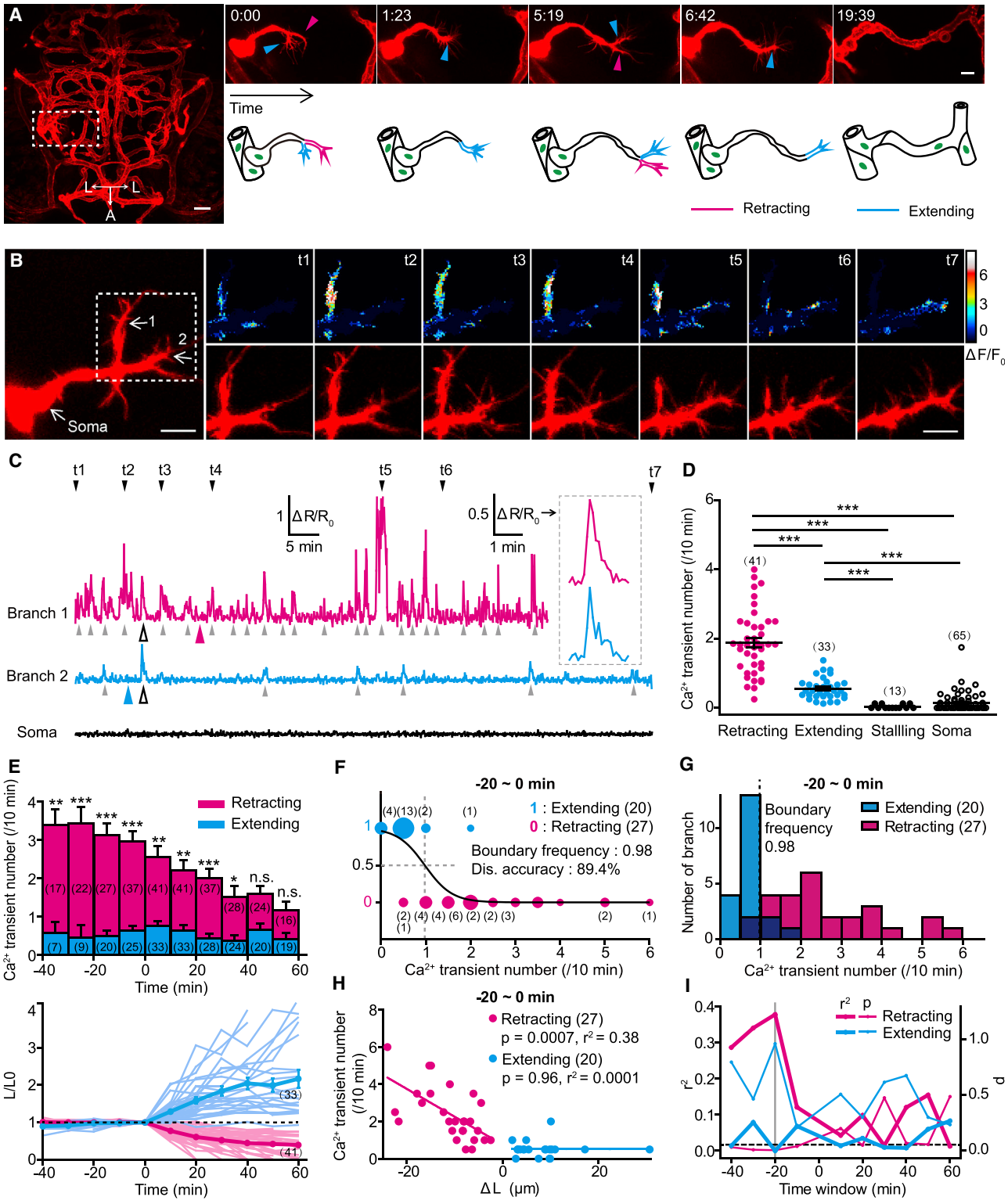

Figure 1. Frequencies of Local Ca^{2+} Transients at Primary Branches of Endothelial Tip Cells Are Correlated with the Fates of Branch Retraction and Extension

(A) Example showing the pathfinding of endothelial tip cells (ETCs) during brain vascular development of zebrafish. Left: projection image of the brain vasculature is shown; right: the pathfinding process for the ETC outlined in the left image is shown. A, anterior; L, lateral.

(legend continued on next page)

axon growth and pathfinding (Gomez and Spitzer, 1999; Gomez and Zheng, 2006; Zheng and Poo, 2007). In terms of vascular development, a few studies showed that Ca^{2+} influx is required for EC proliferation and vessel invasion (Kohn et al., 1995), and VEGF-induced global Ca^{2+} oscillation is associated with EC budding (Savage et al., 2019; Yokota et al., 2015). As wiring of vascular and neural networks shares some common molecular signaling pathways (Andreone et al., 2015; Eichmann et al., 2005; Mackenzie and Ruhrberg, 2012; Tam and Watts, 2010; Wälchli et al., 2015), it is of interest to investigate whether Ca^{2+} is important for ETC pathfinding during vascular development.

Taking advantage of the optical transparency and small size of the brain in larval zebrafish, we performed *in vivo* long-term time-lapse simultaneous imaging of both the morphological dynamics and Ca^{2+} activity of ETCs during brain vascular development. We found that high- and low-frequency sub-cellular Ca^{2+} activities mediated by Piezo1 determine the fate of ETC branch's retraction and extension, respectively, leading to proper pathfinding of ETCs and appropriate patterning of the brain vasculature during development.

RESULTS

ETC Branches Display Morphological Dynamics and Local Ca^{2+} Activities

To visualize the process of ETC pathfinding during brain vascular formation, we carried out *in vivo* time-lapse confocal imaging of transgenic zebrafish Tg(kdrl:HRAS-mCherry) larvae at around 3 days post-fertilization (dpf), in which ECs, including ETCs, express the cell-membrane-bound red fluorescent protein mCherry (Figure 1A). Before reaching target vessels at the middle of the brain, ETCs of growing vessels located at the bi-lateral sides of the brain frequently extended and retracted filopodium-enriching primary branches, leading to continuous changes in the direction of ETC migration and vessel growth (Figures 1A and S1). Then, we performed simultaneous calcium and morphology imaging of ETCs in double transgenic zebrafish Tg(kdrl:GCaMP5,kdrl:HRAS-mCherry) larvae, in which both the GCaMP5 (a genetically encoded Ca^{2+} indicator) and mCherry are specifically expressed in ECs. We found that ETC branches displayed spontaneous local Ca^{2+} transients (Figures 1B and 1C; Video S1).

Frequencies of Local Ca^{2+} Transients Are Correlated with the Fate of ETC Branch's Retraction and Extension

Interestingly, ETC branches destining to or undergoing retraction and extension exhibited relatively high- and low-frequency local Ca^{2+} transients, respectively (Figures 1B–1E and S2; retracting branch versus extending branch: 1.9 ± 0.1 versus 0.6 ± 0.05 per 10 min; $p < 0.001$). Meanwhile, Ca^{2+} transients were rarely observed at stalling branches and somata of ETCs (Figure 1D; stalling branch: 0.04 ± 0.02 per 10 min; soma: 0.1 ± 0.03 per 10 min). We defined the time zero as the start point when branch retraction or extension happened. For retracting branches, local Ca^{2+} transients usually occurred before the beginning of branch retraction and lasted to the late period of retraction process with a declining tendency (magenta in Figure 1E), while for extending branches, Ca^{2+} transients remained at a low level during the entire process (blue in Figure 1E). The amplitude of Ca^{2+} transients occurring at retracting and extending branches had no significant difference (retracting branch versus extending branch: 0.9 ± 0.03 versus 0.8 ± 0.08 $\Delta R/R_0$; $p > 0.05$), and the duration of Ca^{2+} transients at retracting branches was slightly shorter than that at extending branches (retracting branch versus extending branch: 41.0 ± 1.1 s versus 49.6 ± 1.9 s; $p < 0.001$; Figure S3).

Then, we analyzed the relationship between the frequency of local Ca^{2+} activities and the fate of ETC branches by using logistic regression and receiver operating characteristic (ROC). Based on Ca^{2+} activities within 20 min before ("−20–0 min") ETC branch morphological changes, logistic regression analysis showed that the boundary frequency and accuracy for discriminating branch retraction and extension were, respectively, 0.98 per 10 min and 89.4% (Figures 1F and 1G), and the area under ROC curve was 0.94 (1.0 indicating 100% correct discrimination). Similar results were obtained for Ca^{2+} activities within 40 min before ("−40–0 min") ETC branch morphological changes (Figures S4A and S4B; 0.87 per 10 min and 87.5% accuracy for logistic regression analysis and 0.94 for ROC analysis). These results suggest that the frequency of Ca^{2+} transients at ETC branches before morphological changes can predict the fate of ETC branches.

To quantify the correlation between the frequency of local Ca^{2+} transients and the length change of ETC branches, we

(B) Representative images showing simultaneous calcium and morphology imaging of an ETC with two primary branches. Left and right bottom: mCherry signal is shown; right top: color-coded GCaMP5 signal is shown.
(C) Traces of Ca^{2+} activities of the two branches and soma of the ETC shown in (B). Inset: enlarged Ca^{2+} transients from left traces (open arrowheads) are shown. Color arrowhead, time point when branch retraction or extension happened; gray arrowhead, Ca^{2+} transient.
(D) Summary of the mean number of Ca^{2+} transients at the retracting, extending, and stalling branches or soma of ETCs.
(E) Time course of the mean Ca^{2+} transient number (top) and relative length (L/L0, bottom) of retracting and extending ETC branches. The length of the branch measured at the time zero is defined as L0. The light lines represent individual cases, and the heavy lines indicate the average.
(F) Logistic regression analysis of the relationship between the frequency of local Ca^{2+} transients and the fate of ETC branches. The size of the color dots is proportional to the number of events occurred. Dis., discrimination.
(G) Distribution of the frequencies of Ca^{2+} transients at retracting or extending ETC branches. The dashed line indicates the boundary frequency of Ca^{2+} activities calculated in (F). Dark blue bars indicate the overlapped distribution.
(H) Correlation between the frequency of local Ca^{2+} transients and the length change (ΔL) of ETC branches.
(I) Summary of the correlation analysis for both the p and r^2 at different time windows. The dashed horizontal line indicates the p value of 0.05. The gray vertical line indicates the data shown in (H).
The numbers in the brackets indicate the numbers of ETC branches (D–H) or somata (D) examined. Scale bars, 30 μm in left (A) and 10 μm in right (A) and 10 μm in left and right (B). n.s., no significance; *$p < 0.05$; **$p < 0.01$; ***$p < 0.001$ (two-tailed Mann-Whitney test for D; unpaired two-tailed Student's t test for E). Mean ± SEM. See also Figures S1–S4.

further performed linear regression analysis. With respect to retracting branches, the net change of branch length was positively correlated with the frequency of Ca^{2+} transients occurred before, but not after, the beginning of retraction, with a maximal correlation within −20–0 min time window ($r^2 = 0.38$; $p < 0.001$), although for extending branches, there was no significant correlation during the entire period (Figures 1H, 1I, and S4C).

These results together indicate that relatively high- and low-frequency Ca^{2+} transients before branch morphological changes are qualitatively related with the fate of ETC branch's retraction or extension, respectively, and the frequency of Ca^{2+} transients is quantitatively correlated with the degree of ETC branch retraction.

Local Ca^{2+} Transients Are Necessary for the Fate Determination of ETC Branches

To investigate whether local Ca^{2+} transients play a causal role in the fate determination of ETC branches, we then locally manipulated Ca^{2+} concentration at ETC branches and monitored their morphological changes (Figure 2). Ultraviolet (UV)-induced uncaging of the photoactivatable Ca^{2+} chelator Diazo-2 (caged-BAPTA) is an efficient way to spatiotemporally downregulate intracellular Ca^{2+} concentration (Gomez and Spitzer, 1999). We introduced Diazo-2 into larval zebrafish via microinjection at one-cell stage embryos and locally applied 405-nm laser pulses at ETC branches that exhibited high-frequency local Ca^{2+} transients but no obvious morphological change before laser application (Figure 2A). After uncaging of Diazo-2, Ca^{2+} activities were markedly reduced (black in Figures 2B and 2C; before versus after: 2.3 ± 0.2 per versus 0.4 ± 0.1 per 10 min; $p < 0.001$), and targeted ETC branches exhibited no retraction (black in Figure 2D) with a L(30–60)/L0 of 1.01 ± 0.05. Here, the L(30–60) is defined as the branch length within 30–60 min after the uncaging, and the L0 is defined as the branch length at the start point of uncaging. In contrast, for the control group in which solvent, but not Diazo-2, was loaded, ETC branches exhibiting relative high-frequency local Ca^{2+} transients still underwent significant retraction after laser application (magenta in Figure 2D; L(30–60)/L0: 0.6 ± 0.07), and the branch-retraction-associated decrease of Ca^{2+} activity was also observed (magenta in Figure 2C; before versus after: 2.3 ± 0.3 versus 1.4 ± 0.3 per 10 min; $p = 0.07$; see also Figure 1E). As Diazo-2 uncaging could not completely suppress high-frequency Ca^{2+} transients, a minority of targeted ETC branches displayed slight extension after uncaging due to low levels of residual Ca^{2+} transients (see Figures 2C and 2D).

As uncaging of Diazo-2 could not completely abolish Ca^{2+} transients (see Figure 2C), we then locally applied BAPTA AM, a cell-membrane-permeable Ca^{2+} chelator, to ETC branches that exhibited low-frequency Ca^{2+} transients and morphological extension (Figure 2E). In comparison with the control group treated with DMSO (blue in Figures 2F–2H), both Ca^{2+} transients and morphological extension of BAPTM-AM-treated branches were largely suppressed (black in Figures 2F–2H; Ca^{2+} transient frequency before versus after BAPTA AM: 0.6 ± 0.1 versus 0.1 ± 0.05 per 10 min, $p < 0.01$; L(30–60)/L0: BAPTA AM versus DMSO, 1.1 ± 0.06 versus 1.8 ± 0.1, $p < 0.001$). These results indicate that high- and low-frequency local Ca^{2+} activities are necessary for the retraction and extension of ETC branches, respectively.

Local Ca^{2+} Transients Are Sufficient for the Fate Determination of ETC Branches

To examine whether local Ca^{2+} transients are sufficient to determine the fate of ETC branches, we then artificially induced local Ca^{2+} activities at quiescent ETC branches via 405-nm laser-pulse-evoked Ca^{2+} release from NP-EGTA AM/Ca^{2+} complex (Gomez and Spitzer, 1999; Zheng and Poo, 2007), which was locally applied to ETC branches prior to imaging (Figure 2I). At quiescent ETC branches with no obvious Ca^{2+} activity and morphological change, we applied laser pulse stimulation to induce robust Ca^{2+} transients at a relatively high (5 per 10 min) or low (0.5 per 10 min) frequency (Figures 2J, 2K, 2M, and 2N). Induction of Ca^{2+} transients at a frequency of 5 per 10 min (Figure 2K) resulted in ETC branch retraction (Figure 2L; L(30–60)/L0: NP-EGTA AM versus DMSO; 0.6 ± 0.06 versus 1.0 ± 0.1; $p < 0.01$), while induction at a frequency of 0.5 per 10 min (Figure 2N) led to significant extension of ETC branches 10 min after the occurrence of the first induced Ca^{2+} transient (Figure 2O; L(30–60)/L0: NP-EGTA AM versus DMSO; 1.7 ± 0.2 versus 1.1 ± 0.03; $p < 0.01$). These results indicate that high- and low-frequency local Ca^{2+} activities play a sufficient role in determining the fate of ETC branch's retraction and extension, respectively.

Calpain Is Downstream of High-Frequency Local Ca^{2+} Transients in Regulating ETC Branch Retraction

Next, we asked what are downstream of Ca^{2+} activities in determining the fate of ETC branches? Calpain is a protease expressed in eukaryotes that can be activated by a high concentration of Ca^{2+} at millimolar (Cong et al., 1989). Ca^{2+}-influx-induced activation of calpain can disassemble and degenerate focal adhesion proteins anchored on plasma membrane to facilitate cytoskeleton reorganization and contributes to axon and dendrite pruning (Kanamori et al., 2013; Yang et al., 2013). To investigate the involvement of calpain, we suppressed calpain activity in ETCs through bath application of the calpain inhibitor calpeptin (Tsujinaka et al., 1988). We found that neither high- nor low-frequency Ca^{2+} activities of ETC branches were affected by calpain blockade (Figures 3A–3C; $p > 0.5$). However, under calpain blockade, ETC branches displaying high-frequency Ca^{2+} transients did not undergo retraction (black in Figure 3D; L(30–60)/L0: calpeptin versus DMSO; 1.1 ± 0.04 versus 0.3 ± 0.1; $p < 0.001$); meanwhile, ETC branches exhibiting low-frequency Ca^{2+} transients still displayed extension at a similar degree with the control group (Figure 3E; L(30–60)/L0: calpeptin versus DMSO; 1.9 ± 0.1 versus 1.8 ± 0.2; $p = 0.8$). These results indicate that calpain is downstream of high-frequency local Ca^{2+} activities in regulating ETC branch retraction.

NOS Is Downstream of Low-Frequency Local Ca^{2+} Transients in Regulating ETC Branch Extension

Nitric oxide synthase (NOS) is important for the regeneration and pruning of neuronal axons (Song et al., 2019; Rabinovich et al., 2016; Wu et al., 1994), and the maintenance of phosphorylated NOS activity requires Ca^{2+} at micromolar (Yamamoto et al., 2004). We then examined NOS involvement in ETCs pathfinding via bath application of the NOS inhibitor N^G-monomethyl-$_L$-arginine monoacetate (L-NMMA) (Rees et al., 1989). Neither high-

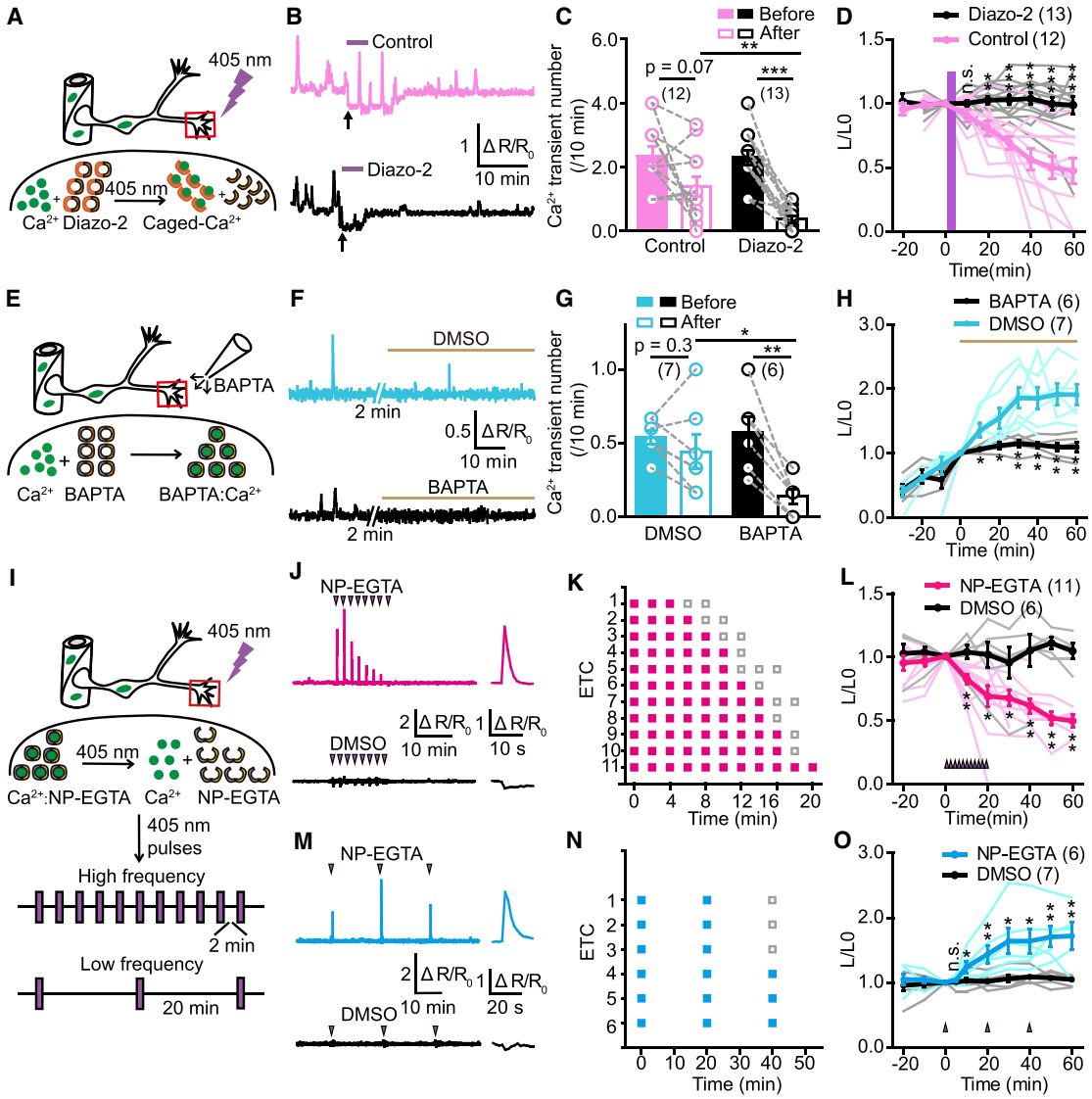

Figure 2. High- and Low-Frequency Local Ca^{2+} Transients of ETC Branches, Respectively, Determine the Fates of Branch Retraction and Extension

(A) Schematic showing application of Diazo-2 focal uncaging to suppress local spontaneous Ca^{2+} activities at ETC branches.

(B–D) Example Ca^{2+} traces (B), summary of Ca^{2+} transient frequencies (C), and time course of the relative length (D) of ETC branches before, during, and after uncaging. The arrows indicate the laser-stimulation-induced immediate photobleaching (B). The purple shapes indicate the laser stimulation (B and D).

(E) Schematic showing local puffing of BAPTA AM to suppress local spontaneous Ca^{2+} activities at ETC branches.

(F–H) Example Ca^{2+} traces (F), summary of Ca^{2+} transient frequencies (G), and time course of the relative length (H) of ETC branches before and during local puffing of BAPTA AM or DMSO. The breaks in the traces indicate the time used for moving the micropipette for puffing to targeted ETC branches (F). The yellow line indicates the period of local puffing (G and H).

(I) Schematic showing focal uncaging of NP-EGTA AM/Ca^{2+} (Ca^{2+}:NP-EGTA) complex to induce local Ca^{2+} increase at quiescent ETC branches.

(J–L) Examples traces (J) and summary for the reliability (K) of Ca^{2+} transients and time course of the relative length (L) of ETC branches induced by laser stimulation (filled triangles) at a relatively high frequency in zebrafish larvae loaded with NP-EGTA AM or DMSO.

(M–O) Examples traces (M) and summary for the reliability (N) of Ca^{2+} transients and time course of the relative length (O) of ETC branches induced by laser stimulation at a relatively low frequency in NP-EGTA AM or DMSO group.

In (K) and (N), each filled square indicates an induced Ca^{2+} transient, each gray open square indicates a failed induction, and each line of the squares represents the data from a single quiescent ETC branch. In (D), (H), (L), and (O), time zero indicates the starting point when manipulations were applied, and the length of the branch measured at the time zero is defined as L0 (unpaired two-tailed Student's t test). In (C) and (G), paired and unpaired two-tailed Student's t test were, respectively, used for intra- and inter-group comparison. *$p < 0.05$; **$p < 0.01$; ***$p < 0.001$. Mean ± SEM.

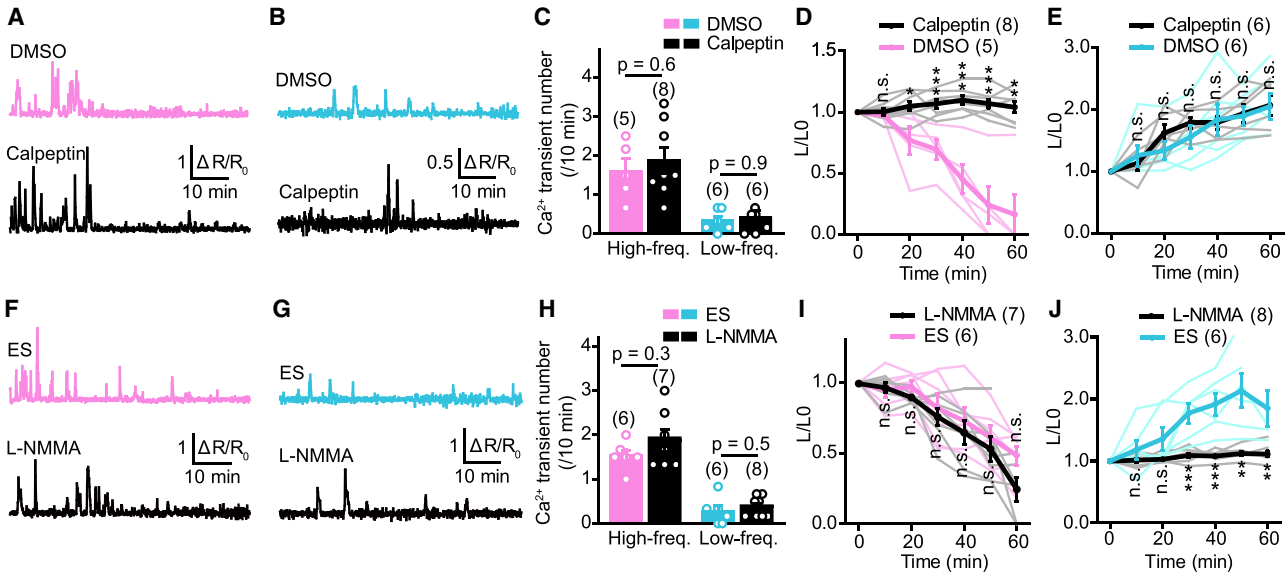

Figure 3. Calpain and NOS Are Downstream of High- and Low-Frequency Local Ca^{2+} Transients in Regulating ETC Branch Retraction and Extension, Respectively

(A–E) Examples (A and B) and summary (C) showing spontaneous local Ca^{2+} activities and time course of the relative length (D and E) of ETC branches under bath application of DMSO or calpeptin.

(F–J) Examples (F and G) and summary (H) showing spontaneous local Ca^{2+} transients and time course of the relative length (I and J) of ETC branches under bath application of external solution (ES) or L-NMMA.

High-freq., high frequency; low-freq., low frequency. *$p < 0.05$; **$p < 0.01$; ***$p < 0.001$ (unpaired two-tailed Student's t test). Mean ± SEM.

nor low-frequency Ca^{2+} activities of ETC branches were affected by NOS blockade (Figures 3F–3H; $p > 0.2$). Under NOS blockade, ETC branches displaying high-frequency Ca^{2+} transients retracted at a similar degree with the control group (Figure 3I; L(30–60)/L0: L-NMMA versus extracellular solution [ES]; 0.6 ± 0.08 versus 0.7 ± 0.07; $p = 0.4$), but ETC branches exhibiting low-frequency Ca^{2+} transients did not undergo extension any more (black in Figure 3J; L(30–60)/L0: L-NMMA versus ES; 1.1 ± 0.03 versus 1.9 ± 0.2; $p < 0.001$), indicating that NOS is downstream of low-frequency local Ca^{2+} activities in regulating ETC branch extension.

Piezo1 Mediates Local Ca^{2+} Transients and Morphological Dynamics of ETC Branches

Next, we asked: what is the origin of local Ca^{2+} activities of ETC branches? Piezos are a family of mechanosensitive and Ca^{2+} permeable non-selective cationic channels (Murthy et al., 2017), of which Piezo1 has been found to involve in mechanical transduction-associated developmental, physiological, and pathological processes, including stem cell differentiation (He et al., 2018), epithelial cell division and extrusion (Gudipaty et al., 2017), neuronal axon growth (Koser et al., 2016) and regeneration (Song et al., 2019), lymphatic valve formation (Nonomura et al., 2018), immune responses (Solis et al., 2019), baroreception (Zeng et al., 2018), ATP-induced vasorelaxation (Wang et al., 2016), and glioma aggression (Chen et al., 2018). In particular, Piezo1 was found to mediate shear stress-induced EC alignment in yolk sac vessels and functional arteries in mice, and loss-of-function of Piezo1 caused EC alignment defects and vascular abnormality (Li et al., 2014; Ranade et al., 2014). We wondered whether Piezo1 can regulate the branch dynamics and associated pathfinding of ETCs via sensing changes in local tissue stiffness and/or cell membrane tension.

Immunostaining showed that Piezo1 was densely expressed in ETC branches in the larval zebrafish brain (Figures 4A and 4B). In *piezo1*$^{-/-}$ knockout zebrafish, which we generated by using the type II bacterial clustered regularly interspaced short palindromic repeats (CRISPR)-CRISPR-associated (Cas) 9 system (CRISPR-Cas9) (Figures S5A and S5B), Piezo1 signal in ETC branches was absent (Figure 4C). Moreover, Ca^{2+} activities at ETC branches in *piezo1*$^{-/-}$ were significantly reduced in comparison with those in wild-type (WT) siblings (Figures 4D and 4E; WT versus *piezo1*$^{-/-}$: 1.0 ± 0.2 versus 0.2 ± 0.05 per 10 min; $p < 0.001$), indicating the requirement of Piezo1 for the generation of local Ca^{2+} activities.

To further demonstrate the role of Piezo1 in local Ca^{2+} transients and morphological dynamics of ETC branches, we then manipulated Piezo1 activity. Piezo1 blockade via local bath application of GsMTx4, a toxin blocker of Piezo1 (Koser et al., 2016), largely suppressed the Ca^{2+} activities of ETC branches exhibiting relatively high-frequency local Ca^{2+} transients (Figures 4F and 4G; $p < 0.01$) and completely prevented the destined retraction of those ETC branches (Figures 4H and S5C; L(30–60)/L0: GsMTx4 versus ES; 1.0 ± 0.09 versus 0.5 ± 0.1; $p < 0.05$). Similarly, Piezo1 blockade also suppressed the Ca^{2+} activities of ETC branches displaying low-frequency local Ca^{2+} transients (Figures 4I and 4J; $p < 0.01$) and impaired the extension of those ETC branches (Figures 4K and S5D;

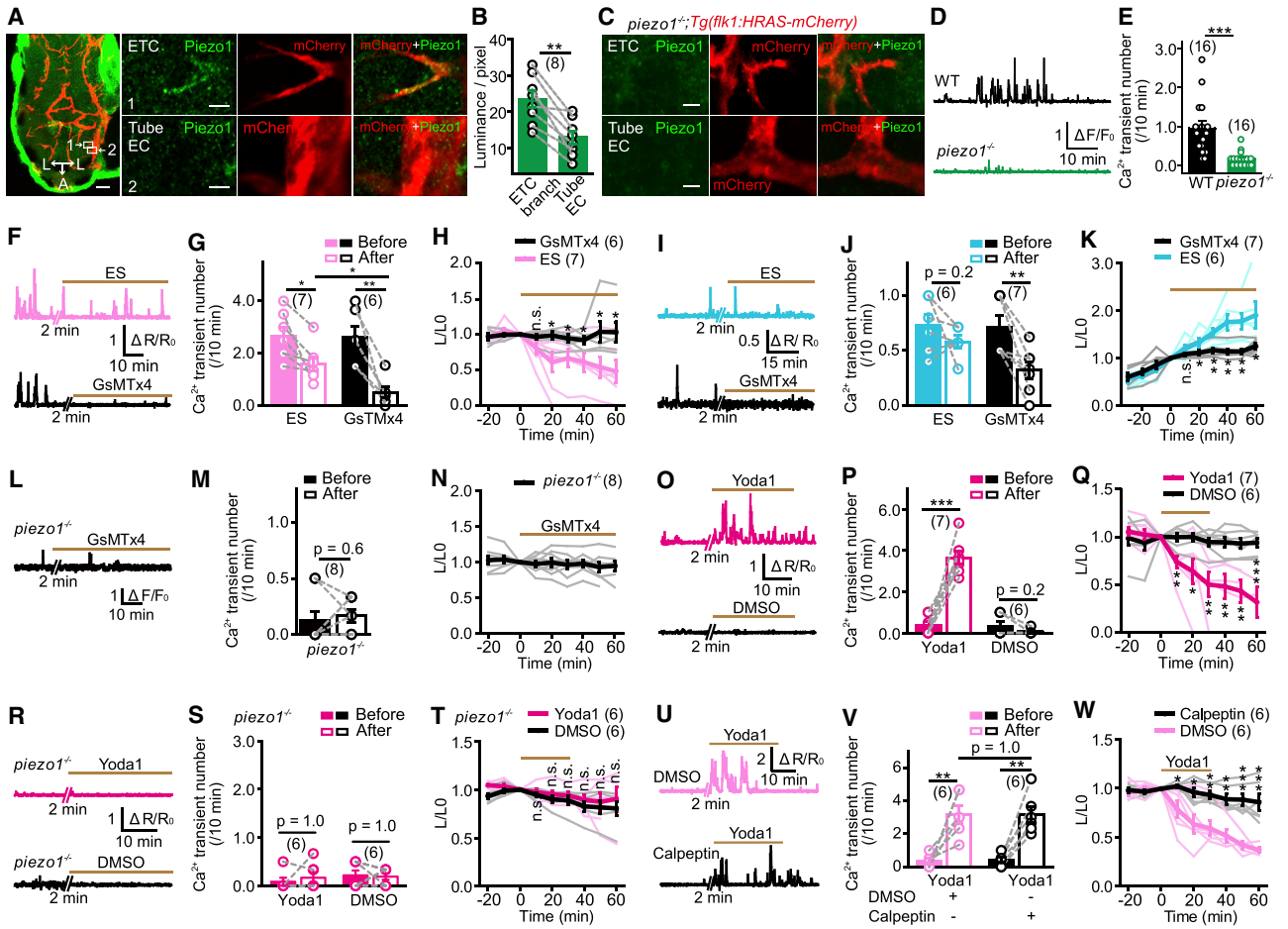

Figure 4. Piezo1 Is Required for Local Ca^{2+} Transients and Retraction/Extension of ETC Branches

(A) Representative images of Piezo1 immunostaining in the brain of a 3-dpf Tg(kdrl:HRAS-mcherry) larval zebrafish. (Left) Projection image of the brain is shown. (Right) Enlarged images (single optical section) outlined in the left are shown. Tube EC, EC located at a vessel tube. Green signals around the brain (left) are due to non-specific staining of the skin. Scale bars, 40 μm (left) and 5 μm (right).

(B) Summary of the relative density of Piezo1 signal at ETC branches and nearby Tube EC. The data were from 8 pairs of ETCs and nearby tube ECs in 5 larvae.

(C) Representative immunostaining of Piezo1 in a 3-dpf *piezo1*$^{-/-}$;Tg(kdrl:HRAS-mcherry) larva. Scale bars, 5 μm.

(D and E) Examples and summary showing local Ca^{2+} activities of ETC branches in Tg(kdrl:GCaMP5) larvae with WT or *piezo1*$^{-/-}$ background. The data were from 16 ETCs in 9 WT siblings and 16 ETCs in 7 *piezo1*$^{-/-}$ larvae.

(F–H) Effects of GsMTx4-mediated Piezo1 blockade on relatively high frequency local Ca^{2+} activities and morphological changes of ETC branches.

(I–K) Effects of GsMTx4-mediated Piezo1 blockade on relatively low frequency local Ca^{2+} activities and morphological changes of ETC branches.

(L–N) Effect of GsMTx4 application on ETC branches in *piezo1*$^{-/-}$ larvae.

(O–Q) Effects of Yoda1-induced Piezo1 activation on local Ca^{2+} activities and morphological dynamics of ETC branches.

(R–T) Effect of Yoda1 application on ETC branches in *piezo1*$^{-/-}$ larvae.

(U–W) Effects of calpeptin-mediated calpain blockade on Yoda1-induced Ca^{2+} activities and morphological changes of ETC branches.

*p < 0.05; **p < 0.01; ***p < 0.001 (paired two-tailed Student's t test for B and M and intra-group comparison in G, J, P, and V; unpaired two-tailed Student's t test for H, K, Q, T, and W and inter-group comparison in G and V; two-tailed Wilcoxon signed rank test for intra-group data comparison in S and two-tailed Mann-Whitney test for E). Mean ± SEM. See also Figure S5.

L(30–60)/L0: GsMTx4 versus ES; 1.2 ± 0.05 versus 1.8 ± 0.2; p < 0.01). As expected, we found that the application of GsMTx4 had no more effect on the Ca^{2+} activity and morphological dynamics of ETC branches in *piezo1*$^{-/-}$ larvae (Figures 4L–4N).

Moreover, the activation of Piezo1 at quiescent ETC branches through puffing of Yoda1, an agonist of Piezo1 (Syeda et al., 2015), induced robust high-frequency local Ca^{2+} transients (Figures 4O and 4P; p < 0.001) and significant retraction of targeted branches of ETCs (Figure 4Q; L(30–60)/L0: Yoda1 versus DMSO; 0.4 ± 0.1 versus 0.9 ± 0.05; p < 0.01). Meanwhile, application of Yoda1 had no effect on the Ca^{2+} activity and morphological dynamics of ETC branches in *piezo1*$^{-/-}$ larvae (Figures 4R–4T), confirming that Yoda1-induced effects on ETC branches are mediated by Piezo1. Furthermore, the blockade of calpain activity by using calpeptin had no significant effect on Yoda1-induced Ca^{2+} activities (Figures 4U and 4V; p = 1.0) but

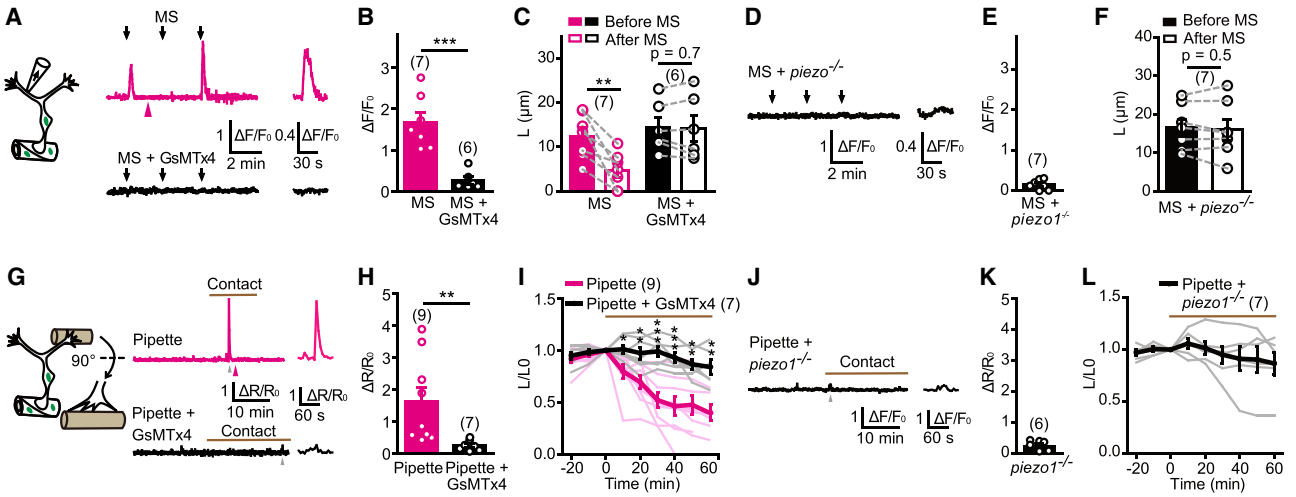

Figure 5. Piezo1 at ETC Branches Is Activated by Mechanical Force

(A) Examples showing Ca^{2+} activities of ETC branches induced by mechanical stretch (MS) (arrow) in animal perfused with ES or GsMTx4. Left: schematic of the MS application is shown; middle: example Ca^{2+} traces are shown; right: averaged Ca^{2+} activities from middle traces are shown.

(B and C) Summary of MS-induced Ca^{2+} activities and ETC branch length before and 10 min after MS.

(D–F) Effect of MS on ETC branches in *piezo1*$^{-/-}$ larvae.

(G) Examples showing Ca^{2+} activities of ETC branches induced by tissue stiffness increase in a larva perfused with ES or GsMTx4. Left: schematic of the application of tissue stiffness increase is shown; middle: example local Ca^{2+} traces are shown; right: enlarged Ca^{2+} transients in the middle are shown.

(H and I) Summary of Ca^{2+} activities and time course of the relative length of ETC branches induced by tissue stiffness increase.

(J–L) Effect of tissue stiffness on ETC branches in *piezo1*$^{-/-}$ larvae.

The filled magenta arrowhead marks the time point when branch retraction occurred in (A) and (G). *p < 0.05; **p < 0.01; ***p < 0.001 (paired and unpaired two-tailed Student's t test, respectively, for C and F and B and I and two-tailed Mann-Whitney test for H). Mean ± SEM. See also Figure S5.

prevented Yoda1-induced retraction of ETC branches (Figure 4W; L(30–60)/L0: calpeptin versus DMSO; 0.9 ± 0.06 versus 0.4 ± 0.08; p < 0.001), confirming that calpain signaling is downstream of Piezo1 activation.

Taken together, these results demonstrate that Pizeo1 expressed at ETC branches is critical for the generation of local Ca^{2+} activities and associated morphological dynamics of ETC branches.

Piezo1 Expressed on ETCs Is Sensitive to Mechanical Force

Mechanical force produced by changes in tissue stiffness, adhesive tension between neighboring cells, or flow-generated frictional force has been reported to play important roles in diverse biological processes, including axon pathfinding (Koser et al., 2016), vessel invasion (Kragl et al., 2016), and EC alignment (Li et al., 2014; Ranade et al., 2014). To determine whether Piezo1 expressed at ETCs acts through its mechanosensitive property, we imposed mechanical stretch ("MS") to the cell membrane of quiescent ETC branches by applying a negative pressure via a micropipette attached to the branch (left in Figure 5A). We found that the mechanical stretch induced very robust local Ca^{2+} activities and morphological retraction of the stimulated ETC branches, and both the Ca^{2+} activities and branch retraction were suppressed by GsMTx4-mediated blockade of Piezo1 (Figures 5A–5C). As expected, application of mechanical stretch on ETC branches in *piezo1*$^{-/-}$ larvae did not induce obvious local Ca^{2+} activity and morphological change (Figures 5D–5F), confirming that the effects of mechanical stretch are mediated by Piezo1.

To further investigate whether tissue stiffness change-associated mechanical force can activate Piezo1 and regulate ETC branch dynamics, we then mimicked a sudden increase of tissue stiffness near the tip of ETC branches through prior embedding of a thick micropipette (left in Figure 5G). We found that ETC branches displayed very strong local Ca^{2+} activities and markedly retracted after contacting the pipette, while GsMTx4-mediated blockade of Piezo1 significantly suppressed the induced Ca^{2+} activities and ETC branch retraction (Figures 5G–5I and S5E; L(30–60)/L0: pipette versus pipette + GsMTx4; 0.5 ± 0.08 versus 0.9 ± 0.05; p < 0.001). Moreover, tissue stiffness increase had no more effect on Ca^{2+} activity and morphology of ETC branches in *piezo1*$^{-/-}$ larvae (Figures 5J–5L), further confirming that the application of increased tissue stiffness is Piezo1 dependent. These results indicate that mechanical forces associated with tissue stiffness changes can activate Piezo1 expressed on ETC branches, leading to local Ca^{2+} activity increases and morphological changes of ETC branches.

Mutating *piezo1* Impairs ETC Pathfinding and Brain Vascular Patterning

To further demonstrate the crucial role of Piezo1 in ETC pathfinding and brain vascular patterning, we first compared the growing path of ETCs in *piezo1*$^{-/-}$ larvae and WT siblings. In comparison with WT siblings, ETCs in *piezo1*$^{-/-}$ possessed more primary branches (Figures 6A and 6B; WT versus *piezo1*$^{-/-}$: 1.7 ± 0.1 versus 3.2 ± 0.3; p < 0.001), and the occurrence of abnormal phenotypes, including connection between two ETCs, connection between ETC branches and parent

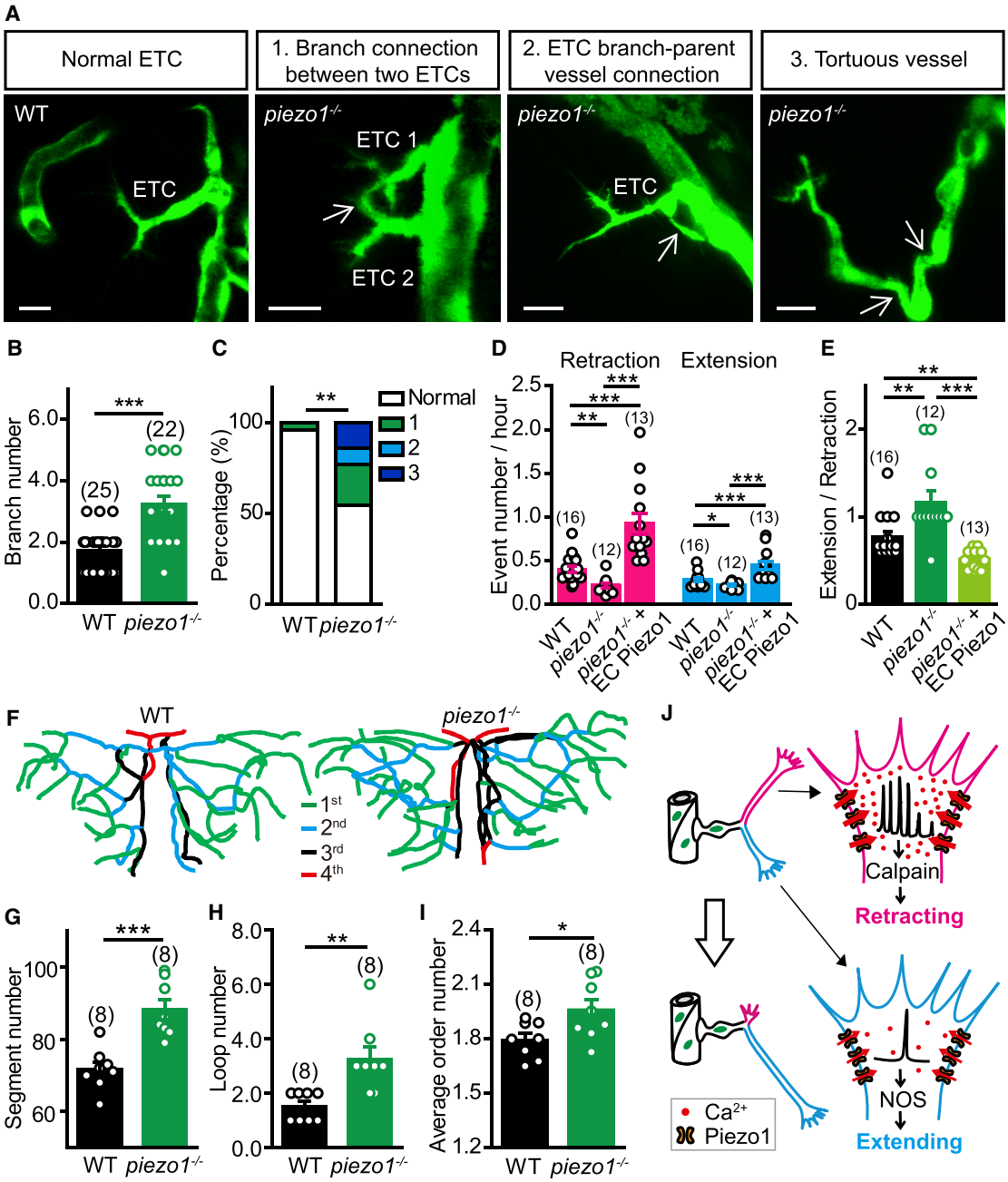

Figure 6. Zebrafish *piezo1* Mutation Impairs ETC Pathfinding and Brain Vascular Patterning

(A) Images of ETC morphology in 3-dpf Tg(kdrl:eGFP) larvae with WT or *piezo1*$^{-/-}$ background. The white arrows indicate abnormal connections. Scale bars, 10 μm.

(B) Summary of the branch number of ETCs in WT siblings and *piezo1*$^{-/-}$ larvae.

(C) Percentages of normal and abnormal morphologies of ETCs and vessels. WT, from 25 ETCs in 12 larvae; *piezo1*$^{-/-}$, from 22 ETCs in 8 larvae.

(D and E) Summary of the retraction and extension (D) and extending/retracting ratio (E) of ETC branches in WT, *piezo1*$^{-/-}$, and *piezo1*$^{-/-}$+EC Piezo1. WT siblings, from 16 ETCs in 9 larvae; *piezo1*$^{-/-}$, from 12 ETCs in 6 larvae; *piezo1*$^{-/-}$+EC Piezo1, from 13 ETCs in 7 larvae.

(F–I) Representative skeletons (F) and summary for the vessel segment number (G), internal vessel loop number (H), and average order number of vessel segments (I) of the midbrain vasculature in WT siblings and *piezo1*$^{-/-}$ larvae at 7 dpf. The numbers in the brackets represent the numbers of larvae examined.

(J) Working model.

The same datasets were used in (B) and (C) or in (D) and (E). *p < 0.05; **p < 0.01; ***p < 0.001 (two-tailed Mann-Whitney test for B, E, and H; Fisher exact test for C; and unpaired two-tailed Student's t test for D, G, and I). Mean ± SEM. See also Figure S6.

vessels, and tortuous vessels, was significantly increased (Figures 6A and 6C; $p < 0.01$). Consistently, using long-term time-lapse imaging of ETCs for 12 h, we further found that the event (per hour) of ETC branch retraction or extension in *piezo1*$^{-/-}$ was significantly reduced (Figure 6D; for retraction, WT versus *piezo1*$^{-/-}$: 0.4 ± 0.04 versus 0.2 ± 0.03 per hour, $p < 0.01$; for extension, WT versus *piezo1*$^{-/-}$: 0.3 ± 0.02 versus 0.2 ± 0.01, $p < 0.05$). As the reduction degree for retraction was larger than that for extension, extending/retracting ratio in *piezo1*$^{-/-}$ was larger than that in WT siblings (Figure 6E; extending/retracting ratio of WT versus *piezo1*$^{-/-}$: 0.8 ± 0.06 versus 1.2 ± 0.1; $p < 0.01$). To further confirm the role of Piezo1 in ECs, we overexpressed Piezo1 specifically in ECs in *piezo1*$^{-/-}$ ("*piezo1*$^{-/-}$+EC Piezo1"; Figure S6). As expected, we found that the occurrence of both ETC branch retraction and extension in larvae of *piezo1*$^{-/-}$+EC Piezo1 was rescued in comparison with *piezo1*$^{-/-}$ and even more frequent than those of WT animals (Figure 6D; for retraction, *piezo1*$^{-/-}$+EC Piezo1: 0.9 ± 0.1 per hour; *piezo1*$^{-/-}$ versus *piezo1*$^{-/-}$+EC Piezo1, $p < 0.001$; WT versus *piezo1*$^{-/-}$+EC Piezo1, $p < 0.001$; for extension, *piezo1*$^{-/-}$+EC Piezo1: 0.4 ± 0.05 per hour, *piezo1*$^{-/-}$ versus *piezo1*$^{-/-}$+EC Piezo1, $p < 0.001$; WT versus *piezo1*$^{-/-}$+EC Piezo1, $p < 0.001$). The extending/retracting ratio was also rescued and even smaller than those in WT animals (Figure 6E; *piezo1*$^{-/-}$+EC Piezo1: 0.5 ± 0.03; *piezo1*$^{-/-}$ versus *piezo1*$^{-/-}$+EC Piezo1, $p < 0.001$; WT versus *piezo1*$^{-/-}$+EC Piezo1, $p < 0.01$). This consistency of morphological and dynamic defects of ETCs in *piezo1*$^{-/-}$ and the rescued effects by EC overexpression of Piezo1 supports the important role of Piezo1 in ETC pathfinding.

To evaluate the defects of *piezo1*$^{-/-}$ on the patterning of the brain vasculature, we quantified the network properties of the brain vasculature using a self-designed Brain Angiotome software (Chen et al., 2012). In comparison with WT siblings, *piezo1*$^{-/-}$ larvae had a more complex brain vasculature (Figure 6F), as evidenced by the increased numbers of vessel segments (Figure 6G; WT versus *piezo1*$^{-/-}$: 71.6 ± 2.0 versus 88.1 ± 2.7; $p < 0.001$), internal vessel loops (Figure 6H; WT versus *piezo1*$^{-/-}$: 1.5 ± 0.2 versus 3.3 ± 0.5; $p < 0.01$), and vessel segment orders (Figure 6I; WT versus *piezo1*$^{-/-}$: 1.8 ± 0.04 versus 2.0 ± 0.06; $p < 0.05$). This increased complexity of the brain vasculature is consistent with the defects in the morphology and dynamics of ETCs in *piezo1*$^{-/-}$.

DISCUSSION

Our study uncovers a novel function of Piezo1 and its downstream Ca^{2+} activity in regulating ETC pathfinding during vascular development in the brain. High- and low-frequency sub-cellular Ca^{2+} activities mediated by the mechanosensitive Piezo1 control ETC branch retraction via calpain or extension via NOS, respectively, resulting in proper ETC pathfinding and vascular patterning (Figure 6J).

Roles of Ca^{2+} Activities in Vascular Development

Ca^{2+} signaling plays versatile roles in regulating axon growth (Gomez and Spitzer, 1999; Gomez and Zheng, 2006; Zheng and Poo, 2007) and dendrite pruning (Kanamori et al., 2013). In this study, we demonstrate that Ca^{2+} is also important for vascular development. Interestingly, we found that local Ca^{2+} activities regulate ETC branch extension or retraction in a frequency-dependent manner. This frequency dependency is somehow similar to the functions of Ca^{2+} in axon growth, because it is known that large elevation of Ca^{2+} leads to slowdown, stalling, or even retraction of axon growth cones, while moderate Ca^{2+} increase accelerates the motility and outgrowth of axon growth cones (Gomez and Spitzer, 1999; Gomez and Zheng, 2006; Zheng and Poo, 2007). Besides local Ca^{2+} activities, we sometimes observed global Ca^{2+} transients appearing in primary branches and somata of ETCs. We speculate that these global activities may contribute to the migration or global growth of ECs. Consistent with this idea, previous studies showed that VEGF can evoke global Ca^{2+} activities and promote EC migration and angiogenic capacity in cultured ECs as well as zebrafish trunk vessels (Noren et al., 2016; Savage et al., 2019; Yokota et al., 2015). Our findings open a door for further understanding of Ca^{2+} activities as an important signal in ETC pathfinding as well as other processes during vascular development and offer a new angle of parallelism between vascular and neural development.

Roles of Piezo1 in ETC Ca^{2+} Activities and Vascular Development

Two previous studies with mice showed that Piezo1 plays a role in EC alignment in yolk sac vessels and arteries via sensing blood-flow-induced shear stress, and loss-of-function of *Piezo1* causes gross defects of vasculatures (Li et al., 2014; Ranade et al., 2014). However, it is unknown about whether and how Piezo1 regulates vascular patterning. In this study, we found that Piezo1 is preferentially expressed on ETC branches and activated by changes of tissue stiffness, leading to increased Ca^{2+} activities and relevant extension/retraction of ETC branches. Meanwhile, *piezo1* mutation impairs the pathfinding of ETCs and disrupts the patterning of the brain vasculature. Thus, our study uncovers that Ca^{2+}-permeable Piezo1 regulates vascular patterning through controlling ETC pathfinding, extending our current understanding of Piezos functions.

Although Piezo1 is not the only mediator of local Ca^{2+} activities and associated morphological dynamics of ETC branches because we still observed sparse Ca^{2+} transients and reduced dynamics of ETC branches after Pizeo1 blockade and/or in *piezo1*$^{-/-}$, our results show that Piezo1 plays a dominant role. First, in ETC branches exhibiting high-frequency local Ca^{2+} activity, application of GsMTx4 reduced the frequency of Ca^{2+} transients from 2.6 ± 0.4 to 0.5 ± 0.2 (see Figure 4G). Meanwhile, in ETC branches exhibiting low-frequency local Ca^{2+} activity, treatment of GsMTx4 decreased the frequency of Ca^{2+} transients from 0.7 ± 0.1 to 0.3 ± 0.1 (see Figure 4J). Thus, Piezo1 accounts for ~81% for high-frequency local Ca^{2+} activity and ~57% for low-frequency local Ca^{2+} activity of ETC branches. It also indicates that Piezo1 contributes more to high-frequency local Ca^{2+} activity than to low-frequency local Ca^{2+} activity. Second, in terms of Piezo1 contribution to the determination of ETC branch fate, the number of retraction events is 0.4 ± 0.04 per hour in WT animals, although it decreases to 0.2 ± 0.03 ($p < 0.01$) in *piezo1*$^{-/-}$ larvae (see Figure 6D). Meanwhile, the

numbers of extension events in WT and *piezo1*$^{-/-}$ larvae are 0.3 ± 0.02 and 0.2 ± 0.01 per hour ($p < 0.05$), respectively (see Figure 6D). These data show that Piezo1 accounts for ~50% for retraction and 33% for extension of ETC branches, consistent with the different degrees of Piezo1 contribution to high- versus low-frequency local Ca^{2+} activities in ETC branches. Third, *piezo1*$^{-/-}$ larvae displayed severe abnormality on vascular patterning (see Figures 6F–6I). Meanwhile Piezo1 overexpression in ECs of *piezo1*$^{-/-}$ completely rescued ETC morphological defects of *piezo1*$^{-/-}$, and the dynamics of ETCs were even enhanced by *piezo1* overexpression in comparison with that of WT animals (see Figure 6D). Taken together, our study demonstrates a critical role of Piezo1 in regulating the dynamics of ETC branches and patterning of the brain vasculature.

It is of interest that Piezo1 can regulate both the retraction and extension of ETC branches via inducing high- and low-frequency Ca^{2+} activities, respectively. It is possible that spontaneous or weak mechanical force-evoked activation of Piezo1 may cause a low level of increase in intracellular Ca^{2+} concentration (Li et al., 2014), which may be necessary for maintaining growth or extension of ETC branches. However, when ETC branches encounter relatively large changes of tissue stiffness or overloading of their membrane tension, more Piezo1 channels can be simultaneously activated, leading to a large increase of intracellular Ca^{2+} concentration and associated retraction of ETC branches. We found that ETC branch retraction was readily induced by the application of Yoda1, mechanical stretch, or tissue stiffness increase (see Figures 4O–4Q and 5), which may cause strong activation of Piezo1 channels under our experimental conditions. Consistently, the degree of Piezo1 activation is positively correlated with the amplitude of mechanical stretch stimuli (Li et al., 2014; Murthy et al., 2017; Ranade et al., 2014), and the activation of calpain and NOS requires, respectively, high and low levels of intracellular Ca^{2+} concentration (Cong et al., 1989; Li et al., 2014; Yamamoto et al., 2004).

ETCs Act as a Sensor for Integrating Mechanical and Chemical Cues during Vascular Development

Tissue stiffness, which is mainly determined by extracellular matrix (ECM) and cellular compartment distribution, provides an important mechanical signal mediating the interaction between cells and microenvironment (Koser et al., 2015, 2016; Swift et al., 2013). For example, local tissue stiffness is critically involved in instructing axon pathfinding in *Xenopus* (Koser et al., 2016). During angiogenesis, ECM stiffness regulates EC branching morphogenesis *in vitro* (Fischer et al., 2009; Myers et al., 2011). In our study, simulated mechanical stretch and tissue stiffness increase can rapidly trigger Piezo1-mediated Ca^{2+} influx and retraction of ETC branches, indicating that ETC branches are sensitive to mechanical signals. It is possible that, during pathfinding, ETC branch-encountered sudden changes in tissue stiffness generated by cell and extracellular matrix distribution activate Piezo1 channels, leading to strong local Ca^{2+} activities and retraction of the branch. Our study suggests that local tissue stiffness and associated mechanical force may act as a guidance cue for the path determination of growing vessels during development.

Vessel growth is a well-coordinated process controlled by multiple microenvironmental factors, including physical cues imposed by surrounding extracellular matrix and chemical cues released by nearby cells or ECs themselves (e.g., VEGF). Previously identified angiogenic factors (including VEGF and Wnt) are found to be required for maintaining the angiogenic capacity of ETCs (Gerhardt et al., 2003, 2004; Geudens and Gerhardt, 2011; James et al., 2009; Martowicz et al., 2019; Savage et al., 2019; Stenman et al., 2008; Wälchli et al., 2015; Yokota et al., 2015). In addition, the anti-angiogenic factor Netrin-1 has been identified to induce retraction of ETC filopodia through the netrin receptor UNC5B expressed in ECs (Lu et al., 2004). In our study, we found that tissue-stiffness-associated mechanical force regulates the path selection of ETCs via controlling the morphological change of their subcellular branches. Through relevant receptors and channels, ETCs can detect and integrate these multiple-modal signals, make a decision for the initiation or direction of growth via coordinating branch retraction and extension, and then steer angiogenic sprouts to target vessels.

STAR★METHODS

Detailed methods are provided in the online version of this paper and include the following:

- KEY RESOURCES TABLE
- RESOURCE AVAILABILITY
  - Lead Contact
  - Materials Availability
  - Data and Code Availability
- EXPERIMENTAL MODEL AND SUBJECT DETAILS
  - Zebrafish Lines
  - Zebrafish husbandry and handling
- METHOD DETAILS
  - Generation of the Tg(kdrl:GCaMP5) Transgenic Zebrafish Line
  - Transient EC-Specific Overexpression of Piezo1 in piezo1$^{-/-}$ Larvae
  - Generation of Zebrafish piezo1$^{-/-}$ via CRISPR/Cas9-Mediated Genome Editing
  - Western Blotting
  - Piezo1 Immunostaining
  - *In Vivo* Confocal Imaging of Intact Zebrafish Larvae
  - Analysis of Calcium Imaging Data
  - Analysis of the Retraction and Extension of ETC Branches
  - Analysis of the Network Properties of the Brain Vasculature
  - Photolysis of Diazo-2 and NP-EGTA
  - Local Puffing and Bath Application of Drugs
  - Application of Mechanical Stimuli
- QUANTIFICATION AND STATISTICAL ANALYSIS

SUPPLEMENTAL INFORMATION

Supplemental Information can be found online at https://doi.org/10.1016/j.neuron.2020.07.025.

ACKNOWLEDGMENTS

We thank Dr. Qian Hu for helping confocal imaging and data analysis of Piezo1 immunostaining, Dr. Hefei Zhang for helping Piezo1 immunostaining, Drs. Jun Yan and Chunfeng Shang for suggestions on logistic regression and receiver operating characteristic analysis, and Dr. Didier Stainier for providing the Tg(kdrl:HRAS-mCherry) and Tg(kdrl:eGFP) lines. This work was supported by Shanghai Municipal Science and Technology Major Project (18JC1410100 and 2018SHZDZX05), Key Research Program of Frontier Sciences (QYZDY-SSW-SMC028) and Strategic Priority Research Program (XDB32010200) of Chinese Academy of Science, and Shanghai Leading Scientist Program.

AUTHOR CONTRIBUTIONS

J.-L.D. supervised the project. T.-T.L. and J.-L.D. designed experiments and wrote the manuscript with inputs from X.-F.D. and S.-Y.G. T.-T.L. performed most experiments except otherwise stated. B.-B.Z. performed some of mechanical stretch experiments. H.-X.Z. and Y.Y. screened *piezo1*$^{-/-}$ founders. J.-A.Y. designed the strategy for generating *piezo1*$^{-/-}$. H.H. wrote the MATLAB code for analyzing Ca^{2+} transients, and Q.C. made the Tg(kdrl:GCaMP5) line.

DECLARATION OF INTERESTS

The authors declare no competing interests.

Received: March 20, 2019
Revised: June 26, 2020
Accepted: July 21, 2020
Published: August 21, 2020

REFERENCES

Adams, R.H., and Alitalo, K. (2007). Molecular regulation of angiogenesis and lymphangiogenesis. Nat. Rev. Mol. Cell Biol. *8*, 464–478.

Adams, S.R., Kao, J.P.Y., and Tsien, R.Y. (1989). Biologically useful chelators that take up calcium(2+) upon illumination. J. Am. Chem. Soc. *111*, 7957–7968.

Akerboom, J., Chen, T.W., Wardill, T.J., Tian, L., Marvin, J.S., Mutlu, S., Calderón, N.C., Esposti, F., Borghuis, B.G., Sun, X.R., et al. (2012). Optimization of a GCaMP calcium indicator for neural activity imaging. J. Neurosci. *32*, 13819–13840.

Andreone, B.J., Lacoste, B., and Gu, C. (2015). Neuronal and vascular interactions. Annu. Rev. Neurosci. *38*, 25–46.

Bae, C., Sachs, F., and Gottlieb, P.A. (2011). The mechanosensitive ion channel Piezo1 is inhibited by the peptide GsMTx4. Biochemistry *50*, 6295–6300.

Balciunas, D., Wangensteen, K.J., Wilber, A., Bell, J., Geurts, A., Sivasubbu, S., Wang, X., Hackett, P.B., Largaespada, D.A., McIvor, R.S., and Ekker, S.C. (2006). Harnessing a high cargo-capacity transposon for genetic applications in vertebrates. PLoS Genet. *2*, e169.

Berridge, M.J., Lipp, P., and Bootman, M.D. (2000). The versatility and universality of calcium signalling. Nat. Rev. Mol. Cell Biol. *1*, 11–21.

Chen, Q., Jiang, L., Li, C., Hu, D., Bu, J.W., Cai, D., and Du, J.L. (2012). Haemodynamics-driven developmental pruning of brain vasculature in zebrafish. PLoS Biol. *10*, e1001374.

Chen, X., Wanggou, S., Bodalia, A., Zhu, M., Dong, W., Fan, J.J., Yin, W.C., Min, H.K., Hu, M., Draghici, D., et al. (2018). A feedforward mechanism mediated by mechanosensitive ion channel PIEZO1 and tissue mechanics promotes glioma aggression. Neuron *100*, 799–815.e7.

Chi, N.C., Shaw, R.M., De Val, S., Kang, G., Jan, L.Y., Black, B.L., and Stainier, D.Y. (2008). Foxn4 directly regulates tbx2b expression and atrioventricular canal formation. Genes Dev. *22*, 734–739.

Cong, J., Goll, D.E., Peterson, A.M., and Kapprell, H.P. (1989). The role of autolysis in activity of the Ca^{2+}-dependent proteinases (μ-calpain and m-calpain). J. Biol. Chem. *264*, 10096–10103.

Eichmann, A., Le Noble, F., Autiero, M., and Carmeliet, P. (2005). Guidance of vascular and neural network formation. Curr. Opin. Neurobiol. *15*, 108–115.

Ellis-Davies, G.C., and Kaplan, J.H. (1994). Nitrophenyl-EGTA, a photolabile chelator that selectively binds Ca^{2+} with high affinity and releases it rapidly upon photolysis. Proc. Natl. Acad. Sci. USA *91*, 187–191.

Esterberg, R., Hailey, D.W., Coffin, A.B., Raible, D.W., and Rubel, E.W. (2013). Disruption of intracellular calcium regulation is integral to aminoglycoside-induced hair cell death. J. Neurosci. *33*, 7513–7525.

Fischer, R.S., Gardel, M., Ma, X., Adelstein, R.S., and Waterman, C.M. (2009). Local cortical tension by myosin II guides 3D endothelial cell branching. Curr. Biol. *19*, 260–265.

Fischer, R.S., Lam, P.Y., Huttenlocher, A., and Waterman, C.M. (2019). Filopodia and focal adhesions: An integrated system driving branching morphogenesis in neuronal pathfinding and angiogenesis. Dev. Biol. *451*, 86–95.

Fluck, R.A. (1995). Responses of the medaka fish egg (Oryzias latipes) to the photolysis of microinjected nitrophenyl-EGTA, a photolabile calcium chelator. Biol. Bull. *188*, 1–4.

Gerhardt, H., Golding, M., Fruttiger, M., Ruhrberg, C., Lundkvist, A., Abramsson, A., Jeltsch, M., Mitchell, C., Alitalo, K., Shima, D., and Betsholtz, C. (2003). VEGF guides angiogenic sprouting utilizing endothelial tip cell filopodia. J. Cell Biol. *161*, 1163–1177.

Gerhardt, H., Ruhrberg, C., Abramsson, A., Fujisawa, H., Shima, D., and Betsholtz, C. (2004). Neuropilin-1 is required for endothelial tip cell guidance in the developing central nervous system. Dev. Dyn. *231*, 503–509.

Geudens, I., and Gerhardt, H. (2011). Coordinating cell behaviour during blood vessel formation. Development *138*, 4569–4583.

Gomez, T.M., and Spitzer, N.C. (1999). In vivo regulation of axon extension and pathfinding by growth-cone calcium transients. Nature *397*, 350–355.

Gomez, T.M., and Zheng, J.Q. (2006). The molecular basis for calcium-dependent axon pathfinding. Nat. Rev. Neurosci. *7*, 115–125.

Gudipaty, S.A., Lindblom, J., Loftus, P.D., Redd, M.J., Edes, K., Davey, C.F., Krishnegowda, V., and Rosenblatt, J. (2017). Mechanical stretch triggers rapid epithelial cell division through Piezo1. Nature *543*, 118–121.

He, L., Si, G., Huang, J., Samuel, A.D.T., and Perrimon, N. (2018). Mechanical regulation of stem-cell differentiation by the stretch-activated Piezo channel. Nature *555*, 103–106.

James, J.M., Gewolb, C., and Bautch, V.L. (2009). Neurovascular development uses VEGF-A signaling to regulate blood vessel ingression into the neural tube. Development *136*, 833–841.

Jin, S.W., Beis, D., Mitchell, T., Chen, J.N., and Stainier, D.Y. (2005). Cellular and molecular analyses of vascular tube and lumen formation in zebrafish. Development *132*, 5199–5209.

Kanamori, T., Kanai, M.I., Dairyo, Y., Yasunaga, K., Morikawa, R.K., and Emoto, K. (2013). Compartmentalized calcium transients trigger dendrite pruning in Drosophila sensory neurons. Science *340*, 1475–1478.

Kashiwagi, S., Izumi, Y., Gohongi, T., Demou, Z.N., Xu, L., Huang, P.L., Buerk, D.G., Munn, L.L., Jain, R.K., and Fukumura, D. (2005). NO mediates mural cell recruitment and vessel morphogenesis in murine melanomas and tissue-engineered blood vessels. J. Clin. Invest. *115*, 1816–1827.

Kohn, E.C., Alessandro, R., Spoonster, J., Wersto, R.P., and Liotta, L.A. (1995). Angiogenesis: role of calcium-mediated signal transduction. Proc. Natl. Acad. Sci. USA *92*, 1307–1311.

Koser, D.E., Moeendarbary, E., Hanne, J., Kuerten, S., and Franze, K. (2015). CNS cell distribution and axon orientation determine local spinal cord mechanical properties. Biophys. J. *108*, 2137–2147.

Koser, D.E., Thompson, A.J., Foster, S.K., Dwivedy, A., Pillai, E.K., Sheridan, G.K., Svoboda, H., Viana, M., Costa, L.D., Guck, J., et al. (2016). Mechanosensing is critical for axon growth in the developing brain. Nat. Neurosci. *19*, 1592–1598.

Kragl, M., Schubert, R., Karsjens, H., Otter, S., Bartosinska, B., Jeruschke, K., Weiss, J., Chen, C., Alsteens, D., Kuss, O., et al. (2016). The biomechanical

properties of an epithelial tissue determine the location of its vasculature. Nat. Commun. *7*, 13560.

Kuhnert, F., Mancuso, M.R., Shamloo, A., Wang, H.T., Choksi, V., Florek, M., Su, H., Fruttiger, M., Young, W.L., Heilshorn, S.C., and Kuo, C.J. (2010). Essential regulation of CNS angiogenesis by the orphan G protein-coupled receptor GPR124. Science *330*, 985–989.

Li, J., Hou, B., Tumova, S., Muraki, K., Bruns, A., Ludlow, M.J., Sedo, A., Hyman, A.J., McKeown, L., Young, R.S., et al. (2014). Piezo1 integration of vascular architecture with physiological force. Nature *515*, 279–282.

Li, J., Zhang, B.B., Ren, Y.G., Gu, S.Y., Xiang, Y.H., and Du, J.L. (2015). Intron targeting-mediated and endogenous gene integrity-maintaining knockin in zebrafish using the CRISPR/Cas9 system. Cell Res. *25*, 634–637.

Lu, X., Le Noble, F., Yuan, L., Jiang, Q., De Lafarge, B., Sugiyama, D., Bréant, C., Claes, F., De Smet, F., Thomas, J.L., et al. (2004). The netrin receptor UNC5B mediates guidance events controlling morphogenesis of the vascular system. Nature *432*, 179–186.

Mackenzie, F., and Ruhrberg, C. (2012). Diverse roles for VEGF-A in the nervous system. Development *139*, 1371–1380.

Martowicz, A., Trusohamn, M., Jensen, N., Wisniewska-Kruk, J., Corada, M., Ning, F.C., Kele, J., Dejana, E., and Nyqvist, D. (2019). Endothelial β-catenin signaling supports postnatal brain and retinal angiogenesis by promoting sprouting, tip cell formation, and VEGFR (vascular endothelial growth factor receptor) 2 expression. Arterioscler. Thromb. Vasc. Biol. *39*, 2273–2288.

Murthy, S.E., Dubin, A.E., and Patapoutian, A. (2017). Piezos thrive under pressure: mechanically activated ion channels in health and disease. Nat. Rev. Mol. Cell Biol. *18*, 771–783.

Myers, K.A., Applegate, K.T., Danuser, G., Fischer, R.S., and Waterman, C.M. (2011). Distinct ECM mechanosensing pathways regulate microtubule dynamics to control endothelial cell branching morphogenesis. J. Cell Biol. *192*, 321–334.

Nonomura, K., Lukacs, V., Sweet, D.T., Goddard, L.M., Kanie, A., Whitwam, T., Ranade, S.S., Fujimori, T., Kahn, M.L., and Patapoutian, A. (2018). Mechanically activated ion channel PIEZO1 is required for lymphatic valve formation. Proc. Natl. Acad. Sci. USA *115*, 12817–12822.

Noren, D.P., Chou, W.H., Lee, S.H., Qutub, A.A., Warmflash, A., Wagner, D.S., Popel, A.S., and Levchenko, A. (2016). Endothelial cells decode VEGF-mediated Ca^{2+} signaling patterns to produce distinct functional responses. Sci. Signal. *9*, ra20.

Padget, D.H. (1956). The cranial venous system in man in reference to development, adult configuration, and relation to the arteries. Am. J. Anat. *98*, 307–355.

Rabinovich, D., Yaniv, S.P., Alyagor, I., and Schuldiner, O. (2016). Nitric oxide as a switching mechanism between axon degeneration and regrowth during developmental remodeling. Cell *164*, 170–182.

Ranade, S.S., Qiu, Z., Woo, S.H., Hur, S.S., Murthy, S.E., Cahalan, S.M., Xu, J., Mathur, J., Bandell, M., Coste, B., et al. (2014). Piezo1, a mechanically activated ion channel, is required for vascular development in mice. Proc. Natl. Acad. Sci. USA *111*, 10347–10352.

Rees, D.D., Palmer, R.M., Hodson, H.F., and Moncada, S. (1989). A specific inhibitor of nitric oxide formation from L-arginine attenuates endothelium-dependent relaxation. Br. J. Pharmacol. *96*, 418–424.

Savage, A.M., Kurusamy, S., Chen, Y., Jiang, Z., Chhabria, K., MacDonald, R.B., Kim, H.R., Wilson, H.L., van Eeden, F.J.M., Armesilla, A.L., et al. (2019). tmem33 is essential for VEGF-mediated endothelial calcium oscillations and angiogenesis. Nat. Commun. *10*, 732.

Solis, A.G., Bielecki, P., Steach, H.R., Sharma, L., Harman, C.C.D., Yun, S., de Zoete, M.R., Warnock, J.N., To, S.D.F., York, A.G., et al. (2019). Mechanosensation of cyclical force by PIEZO1 is essential for innate immunity. Nature *573*, 69–74.

Song, Y., Li, D., Farrelly, O., Miles, L., Li, F., Kim, S.E., Lo, T.Y., Wang, F., Li, T., Thompson-Peer, K.L., et al. (2019). The mechanosensitive ion channel Piezo inhibits axon regeneration. Neuron *102*, 373–389.e6.

Stenman, J.M., Rajagopal, J., Carroll, T.J., Ishibashi, M., McMahon, J., and McMahon, A.P. (2008). Canonical Wnt signaling regulates organ-specific assembly and differentiation of CNS vasculature. Science *322*, 1247–1250.

Swift, J., Ivanovska, I.L., Buxboim, A., Harada, T., Dingal, P.C., Pinter, J., Pajerowski, J.D., Spinler, K.R., Shin, J.W., Tewari, M., et al. (2013). Nuclear lamin-A scales with tissue stiffness and enhances matrix-directed differentiation. Science *341*, 1240104.

Syeda, R., Xu, J., Dubin, A.E., Coste, B., Mathur, J., Huynh, T., Matzen, J., Lao, J., Tully, D.C., Engels, I.H., et al. (2015). Chemical activation of the mechanotransduction channel Piezo1. eLife *4*, e07369.

Tam, S.J., and Watts, R.J. (2010). Connecting vascular and nervous system development: angiogenesis and the blood-brain barrier. Annu. Rev. Neurosci. *33*, 379–408.

Tsujinaka, T., Kajiwara, Y., Kambayashi, J., Sakon, M., Higuchi, N., Tanaka, T., and Mori, T. (1988). Synthesis of a new cell penetrating calpain inhibitor (calpeptin). Biochem. Biophys. Res. Commun. *153*, 1201–1208.

Wälchli, T., Pernet, V., Weinmann, O., Shiu, J.Y., Guzik-Kornacka, A., Decrey, G., Yüksel, D., Schneider, H., Vogel, J., Ingber, D.E., et al. (2013). Nogo-A is a negative regulator of CNS angiogenesis. Proc. Natl. Acad. Sci. USA *110*, E1943–E1952.

Wälchli, T., Wacker, A., Frei, K., Regli, L., Schwab, M.E., Hoerstrup, S.P., Gerhardt, H., and Engelhardt, B. (2015). Wiring the vascular network with neural cues: a CNS perspective. Neuron *87*, 271–296.

Wang, S., Chennupati, R., Kaur, H., Iring, A., Wettschureck, N., and Offermanns, S. (2016). Endothelial cation channel PIEZO1 controls blood pressure by mediating flow-induced ATP release. J. Clin. Invest. *126*, 4527–4536.

Wu, H.H., Williams, C.V., and McLoon, S.C. (1994). Involvement of nitric oxide in the elimination of a transient retinotectal projection in development. Science *265*, 1593–1596.

Xu, B., Zhang, Y., Du, X.F., Li, J., Zi, H.X., Bu, J.W., Yan, Y., Han, H., and Du, J.L. (2017). Neurons secrete miR-132-containing exosomes to regulate brain vascular integrity. Cell Res. *27*, 882–897.

Yamamoto, Y., Katsumata, O., Furuyama, S., and Sugiya, H. (2004). Ca^{2+}, calmodulin and phospholipids regulate nitricoxide synthase activity in the rabbit submandibular gland. J. Comp. Physiol. B *174*, 593–599.

Yang, J., Weimer, R.M., Kallop, D., Olsen, O., Wu, Z., Renier, N., Uryu, K., and Tessier-Lavigne, M. (2013). Regulation of axon degeneration after injury and in development by the endogenous calpain inhibitor calpastatin. Neuron *80*, 1175–1189.

Yokota, Y., Nakajima, H., Wakayama, Y., Muto, A., Kawakami, K., Fukuhara, S., and Mochizuki, N. (2015). Endothelial Ca^{2+} oscillations reflect VEGFR signaling-regulated angiogenic capacity in vivo. eLife *4*, e08817.

Yu, P.C., Gu, S.Y., Bu, J.W., and Du, J.L. (2010). TRPC1 is essential for in vivo angiogenesis in zebrafish. Circ. Res. *106*, 1221–1232.

Zeng, W.Z., Marshall, K.L., Min, S., Daou, I., Chapleau, M.W., Abboud, F.M., Liberles, S.D., and Patapoutian, A. (2018). PIEZOs mediate neuronal sensing of blood pressure and the baroreceptor reflex. Science *362*, 464–467.

Zheng, J.Q., and Poo, M.M. (2007). Calcium signaling in neuronal motility. Annu. Rev. Cell Dev. Biol. *23*, 375–404.

Zhu, J., Motejlek, K., Wang, D., Zang, K., Schmidt, A., and Reichardt, L.F. (2002). beta8 integrins are required for vascular morphogenesis in mouse embryos. Development *129*, 2891–2903.

Zlokovic, B.V. (2008). The blood-brain barrier in health and chronic neurodegenerative disorders. Neuron *57*, 178–201.

STAR★METHODS

KEY RESOURCES TABLE

REAGENT or RESOURCES	SOURCE	IDENTIFIER
Antibodies		
Goat polyclonal anti-Piezo1	Santa Cruze	Cat #: sc-164319; RRID: AB_10842990
Alexa 488 donkey anti-goat IgG secondary antibody	Thermo Fisher Scientific	Cat #: A-11055; RRID: AB_2534102
Donkey anti-goat IgG (HRP)	Abcam	Cat #: ab97110; RRID: AB_10679463
Mouse monoclonal anti-α-tublin	Sigma	Cat #: T6199; RRID: AB_477583
Goat anti-Mouse IgG (HRP)	Invitrogen	Cat #: A16066; RRID: AB_2534739
Chemicals, Peptides, and Recombinant Proteins		
BAPTA AM	Thermo Fisher Scientific	Cat #: B1205
Calpeptin	Sigma-Aldrich	Cat #: C8999
Diazo-2	Molecular Probes	Cat #: D3034
GsMTx4	Abcam	Cat #: Ab141871
L-NMMA	Sigma-Aldrich	Cat #: M7033
NP-EGTA AM	Molecular Probes	Cat #: N6803
Pluronic F-127	Molecular Probes	Cat #: P3000
1-phenyl-2-thiourea (PTU)	Sigma-Aldrich	Cat #: P629
TTX	Tocris Bioscience	Cat #: 1078
Vybrant® DiO cell-labeling solution	Thermo Fisher Scientific	Cat #: V22886
Yoda1	Tocris Bioscience	Cat #: 5586
α-bungarotoxin	Tocris Bioscience	Cat #: 2133
Cas9 nuclease	New England BioLabs	Cat #: M0386S
RIPA lysis buffer	Beyotime	Cat #: P0013D
Cocktail	Sigma	Cat #: P1860
PMSF	Sigma	Cat #: 10837091001
Immobilon Western HRP substrate	Millipore	Cat #: WBKLS0500
Blocking regent	Roche	Cat #: 11096176001
Fluorescent mounting medium	Dako North America	Cat #: S3023
Critical Commercial Assays		
MAXIscript T7 kit	Ambion	Cat #: AM1312M
mirVana miRNA isolation kit	Ambion	Cat #: AM1560
Experimental Models: Organisms/Strains		
Zebrafish: Tg(kdrl:HRAS-mCherry)	Chi et al., 2008	ZFIN ID: ZDB-ALT-081212-4
Zebrafish: Tg(kdrl:eGFP)	Jin et al., 2005	ZFIN ID: ZDB-ALT-050916-14
Zebrafish: Tg(kdrl:GCaMP5)	This paper	N/A
Zebrafish: *piezo1*$^{-/-}$	This paper	N/A
Oligonucleotides		
GCTCAGTGTGGTCAACCCGG	This paper	Piezo1 sgRNA targeting sequence
GAAGCTGCTGTGGCCATCACGCTTTCCATGTGCTTG	This paper	Primers for *piezo1* mutant genotyping, Forward
GTCATATATCGCCCATCCCTA	This paper	Primers for *piezo1* mutant genotyping, Reverse
Software and Algorithms		
ImageJ	National Institute of Health, USA	https://imagej.nih.gov/ij/index.html
Self-written MATLAB program to discriminate Ca^{2+} transients	This paper	N/A
Self-designed Brain Angiotome software	Chen et al., 2012	N/A

RESOURCE AVAILABILITY

Lead Contact

Further information and requests for resources and reagents should be directed to and will be fulfilled by the Lead Contact, Jiu-lin Du (forestdu@ion.ac.cn).

Materials Availability

All unique/stable reagents generated in this study, including transgenic lines, mutants, and plasmids, are available from the Lead Contact without restriction.

Data and Code Availability

Code for data analysis generated in this study is available from the Lead Contact without restriction. No dataset is generated for public repositories in this study.

EXPERIMENTAL MODEL AND SUBJECT DETAILS

Zebrafish Lines

Zebrafish larvae at 3 or 7 days post-fertilization (dpf) were used for all experiments in this study. As the sex of zebrafish is not specified at larval stages, sex discrimination was not included in our study. Zebrafish larvae of Tg(kdrl:eGFP) (Jin et al., 2005) with wild-type (WT) or *piezo1*$^{-/-}$ background at 7 dpf were used for brain vasculature imaging experiments in this study. Zebrafish larvae of Tg(kdrl:HRAS-mCherry) (Chi et al., 2008), Tg(kdrl:GCaMP5,kdrl:HRAS-mCherry), Tg(kdrl:eGFP) (Jin et al., 2005) with wild-type (WT) or *piezo1*$^{-/-}$ background, and Tg(kdrl:GCaMP5) with WT or *piezo1*$^{-/-}$ background at 3 dpf were used for other experiments in the study.

Zebrafish husbandry and handling

Adult zebrafish were maintained in the National Zebrafish Resources of China (NZRC, Shanghai, China) with an automatic fish housing system at 28°C following a standard protocol (Chen et al., 2012; Yu et al., 2010). Embryos were raised under a 14 h/10 h light/dark cycle in 10% Hank's solution, which consisted of (in mM): 140 NaCl, 5.4 KCl, 0.25 Na_2HPO_4, 0.44 KH_2PO_4, 1.3 $CaCl_2$, 1.0 $MgSO_4$ and 4.0 $NaHCO_3$ (pH 7.2), and 1-phenyl-2-thiourea (PTU, P629, Sigma) was added to the solution with a final concentration of 0.003% (w/v) to prevent pigment formation at 1 dpf. Handling procedures were approved by the Institute of Neuroscience, Chinese Academy of Sciences.

METHOD DETAILS

Generation of the Tg(kdrl:GCaMP5) Transgenic Zebrafish Line

To generate a *pminiTol2-kdrl-GCaMP5* construct, the DNA sequence of the 6429-bp *kdrl* promoter (Jin et al., 2005) and the 1353-bp cDNA of *GCaMP5* (Akerboom et al., 2012) were amplified, and then inserted into a 4578-bp *pminiTol2* transposon coding sequence-containing vector (Balciunas et al., 2006). The construct was confirmed by sequencing. The *pminiTol2-kdrl-GCaMP5* construct (dosage of 25 ng/μl) was then co-injected with Tol2 transposase mRNA (dosage of 25 ng/μl) into one-cell stage WT embryos to make Tg(kdrl:GCaMP5) transgenic lines.

Transient EC-Specific Overexpression of Piezo1 in piezo1$^{-/-}$ Larvae

To generate the *yTol2-kdrl-piezo1-EGFP* construct, we optimized a *yTol2* transposon-coding sequence based on the *pminiTol2*. The DNA coding sequences of 7620-bp zebrafish *piezo1* and 720-bp *EGFP* were amplified, and then inserted into a 10182-bp *yTol2-kdrl* containing vector. Afterward, the construct was confirmed by sequencing, and then co-injected (dosage of 25 ng/μl) with Tol2 transposase mRNA (dosage of 25 ng/μl) into one-cell stage *piezo1*$^{-/-}$;Tg(kdrl:HRAS-mCherry) embryos.

Generation of Zebrafish piezo1$^{-/-}$ via CRISPR/Cas9-Mediated Genome Editing

The *piezo1* knock-out zebrafish line was generated by using CRISPR/Cas9-mediated genome editing as previously described (Li et al., 2015). The single guide RNA (sgRNA) targeting the sequence of the zebrafish *piezo1* was designed at the exon 19, which is before the sequence for encoding the critical Piezo domain. This targeting strategy was previously used to make *Piezo1* knockout mice (Li et al., 2014; Ranade et al., 2014). The sgRNA targeting sequence is 5′ - GCTCAGTGTGGTCAACCCGG - 3′. The single-strand DNA containing the *piezo1* sgRNA sequence was annealed and cloned into a pT7-gRNA plasmid. Then the sgRNA was transcribed with the MAXIscript T7 kit (Ambion, AM1312M) and purified with the mirVana miRNA isolation kit (Ambion, AM1560). The *Cas9* nuclease (600 pg, NEB, M0386S) and the *piezo1* gRNA (40 ng) were co-injected into WT zebrafish embryos at one-cell stage.

Mutations of the zebrafish *piezo1* in embryos were examined by PCR and sequencing analysis with primers (Forward: 5′ - GAA GCTGCTGTGGCCATCACGCTTTCCATGTGCTTG - 3′; Reverse: 5′ - GTCATATATCGCCCATCCCTA - 3′). A *piezo1* mutation was identified with a 2 bp deletion in the exon 19. The mutation leads to frameshift and premature stop (in the exon 20) of *piezo1*. The

adult F0 founder carrying the *piezo1* mutation was then crossed with the Tg(kdrl:eGFP), Tg(kdrl:GCaMP5), or Tg(kdrl:HRAS-mCherry) to generate *piezo1*$^{+/-}$;Tg(kdrl:eGFP), *piezo1*$^{+/-}$;Tg(kdrl:GCaMP5), or *piezo1*$^{+/-}$;Tg(kdrl:HRAS-mCherry) lines. After imaging experiments, embryos produced by those adult zebrafish were genotyped to discriminate WT, heterozygous, or homozygous identity.

Western Blotting

WT or *piezo1*$^{-/-}$ zebrafish larvae at 3 dpf were lysed in the RIPA (P0013D, Beyotime) solution containing protease inhibitor Cocktail (P1860, Sigma) and PMSF (10837091001, Sigma). Equal amounts of protein samples were separated with SDS-PAGE (8%), and transferred onto PVDF membranes. Membranes were then incubated by the blocking solution (5% BSA, 0.1% Tween-20, in TBS) for 2 hr at room temperature, and further incubated with primary antibodies for Piezo1 (1:500, sc-164319, Santa Cruze) or α-Tublin (1:5000, T6199, Sigma) overnight at 4°C. After 3 × 15 min wash with TBST buffer (0.1% Tween-20, in TBS), the membranes were incubated with HRP-conjugated secondary antibodies for 2 hr at room temperature, followed by rewash and signal detection with Immobilon Western HRP substrate (WBKLS0500, Millipore).

Piezo1 Immunostaining

Tg(kdrl:HRAS-mCherry) larvae at 3 dpf were fixed with 4% paraformaldehyde (PFA) overnight at 4°C under the darkness. After 4 × 10 min wash with the PBST buffer (PBS + 0.1% Triton X-100), the larvae were mounted with 4% low-melting point agarose. The larvae were then horizontally sliced (100 μm in thickness). The slices were incubated in a solution containing 150 mM Tris-HCl and 0.5% SDS (pH 8.8) for 30 min at 70°C to facilitate antigen retrieval. Then the slices were washed twice with PBST and further dehydrated with acetone for 30 min at −20°C. After wash with PBST 4 times, the slices were incubated in the blocking solution (Composition: blocking regents (1:10, 11096176001, Roche), 0.1% Tween-20 and 0.5% Triton X-100, in PBS) for 2 hr at room temperature, followed by incubation with a goat anti-Piezo1 primary antibody (1:100, sc-164319, Santa Cruze) dissolved in the blocking solution overnight at 4°C. After wash with PBST for 4 times, the slices were incubated with an Alexa 488 donkey anti-goat IgG secondary antibody (1:1000, A-11055, Thermo Fisher) dissolved in the blocking solution under the darkness for 2 hr at room temperature. After wash with PBST for 4 times, the slices were coated onto slides, sealed with a fluorescent mounting medium (S3023, DAKO), and covered by coverslips for confocal imaging with Z axis resolution of 1 μm.

In Vivo Confocal Imaging of Intact Zebrafish Larvae

Monitoring of the morphology of endothelial tip cells (ETC) and patterning of the brain vasculature was carried on Tg(kdrl:HRAS-mCherry) or Tg(kdrl:eGFP) larvae, and simultaneous monitoring of the Ca^{2+} activity and morphology of ETCs was carried on Tg(kdrl:GCaMP5,kdrl:HRAS-mCherry) larvae. *In vivo* imaging experiments were performed by using a Nikon FN1 confocal microscope equipped with a 25 × (NA 1.1) or 40 × (NA 0.8) water-immersion objective. Before imaging, larvae were immobilized in 1.2% low-melting point agarose. The agarose around the larva's mouth and tail was removed to leave space for growing. Three-dimensional time-series calcium imaging was done at the incubation temperature of about 28°C via a heating system, with a Z axis resolution of 4 μm. Laser beams of 488 nm and 561 nm were used to excite GCaMP5 (for Ca^{2+} activity) and mCherry (for morphology) of endothelial tip cells (ETC), respectively. ETCs budding from the choroidal vascular plexus (CVP), which locates peripherally in the midbrain, and then migrating into the midbrain were selected for imaging.

Analysis of Calcium Imaging Data

Ratiometric analysis of Ca^{2+} activities in Tg(kdrl:GCaMP5,kdrl:HRAS-mCherry) larvae was performed with ImageJ (NIH). Z axis projected images within the same series were aligned along X-Y plane by using the plugin of Translation Transformation. The region of interest (ROI) was drawn manually to outline the intact morphology of ETC branches, and the gray-scale value of each ROI was quantified as F. The ratio of $F_{GCaMP5}/F_{mCherry}$ was defined as R. The averaged value of the first 100 frames from ascending ordered R was defined as R_0. $(R-R_0)/R_0$ was then calculated and the value larger than 3 times of standard deviation was identified as a Ca^{2+} transient.

To calculate the peak magnitude, duration and number of Ca^{2+} transients, a self-written MATLAB program was used. As Ca^{2+} activities of ETCs were non-stereotypical while the baseline was subject to fluctuation during *in vivo* long-term imaging, we used an adaptive and iterative algorithm to discriminate Ca^{2+} transients. We first decided which data points should be included in the baseline set, denoted as B, by iteratively removing potential Ca^{2+} transients from the candidate baseline set as follows.

1) Initialized the baseline set B_0 as the full-length raw Ca^{2+} data by $B_0 = \{x(t): t \in [0,T]\}$, where T is the total length of the recording;
2) Starting from n = 0, calculated the smoothed baseline B'_n by running a moving average filter (100 s width) across the data points in B_n (ignoring any gaps due to removed data points in previous steps);
3) Calculated the standard deviation σ_n of the baseline residuals by $\sigma_n = \mathrm{std}(B_n - B'_n)$;
4) Generated B_{n+1} by removing data points from B_n which were larger than $B'_n + 3\sigma_n$ by $B_{n+1} = B_n \backslash \{x(t): x(t) \in B_n, x(t) > B'_n(t) + 3\sigma_n\}$;
5) Repeated steps 2 - 4 until convergence of B, i.e., $B_{N+1} = B_N$, or no more data points should be removed in step 4 (typically within 20 iterations).

After the above steps, we obtained the set of potential Ca^{2+} transients $C = B_0 \setminus B_N$, which consisted of all the data points that had been removed from B_0 during the iteration. We then defined actual Ca^{2+} transients as those with duration longer than 15 s in C. To

further quantify Ca^{2+} transients, we derived the final full-length baseline trace through filling the gaps in the smoothed baseline B_N' by linear interpolation and subtracted the final baseline trace from the raw data B_0. All the relevant analyses were based on this final-baseline-subtracted Ca^{2+} trace.

Analysis of the Retraction and Extension of ETC Branches

To calculate the length of ETC branches, the branch was first traced by defining the start (root) and end (tip) points of the calculated branch on the Z-projected mCherry image by using the plugin of Simple Neurite Tracer in ImageJ, and then the branch length was measured. The retraction or extension of ETC branches were defined by an increase or decrease in the length above 2 μm within 60 min. To characterize the final fate of retraction or extension of ETC branches in long-term time-lapse imaging (12 hr) (see Figure 6D), one existing branch that disappeared completely in the following imaging period was counted as one event of branch retraction, and one existing branch that underwent length increase larger than 2 μm or new daughter branch formation was counted as one event of branch extension.

Analysis of the Network Properties of the Brain Vasculature

To characterize the network properties of three-dimensional brain vasculatures, a self-designed Brain Angiotome software was used as described previously (Chen et al., 2012). Briefly, the three-dimensional skeleton of the midbrain vasculature was extracted following sequential steps of de-convolution, segmentation and skeleton generation. Then the vessel segment number, internal vessel loop number and averaged vessel segment order were calculated. The first order segments were defined as the segments directly connecting with the CVP, and the sequential order numbers of segments were assigned by the Strahler ordering method. The segment order and internal loop numbers were used to reflect the complexity of the midbrain vascular network.

Photolysis of Diazo-2 and NP-EGTA

Focal photolysis of Diazo-2 was applied to inhibit local Ca^{2+} transients of ETC branches. The working solution of Diazo-2 (25 mM, D3034, Molecular Probes) dissolved in a solution containing (in mM) 100 KCl, 10 EGTA, and 10 3-(*N*-morpholino) propanesulfonic acid (MOPS) (pH 7.2) was micro-injected into one-cell stage embryos with a dosage of 1 nL under the red-light illumination as previously reported (Adams et al., 1989; Esterberg et al., 2013; Gomez and Spitzer, 1999), and the embryos were kept under the darkness until uncaging of Diazo-2 was conducted. Before uncaging, spontaneous Ca^{2+} activities and morphological dynamics of ETC branches were monitored for 10 - 30 min, and those exhibiting not less than 4 Ca^{2+} events and no obvious morphological change were selected for uncaging stimulation. Local photolysis of Diazo-2 in a ~6 × 6 μm square at the tip region of the target ETC branch was accomplished with a 405-nm UV laser. The power of the laser was 0.36 mW. The pattern contains 30 cycles, and each cycle consists of spaced photolysis and Ca^{2+} imaging with a duration of 5 s each. For each cycle of photolysis, there is 40 scan pulses (8 pulses per second). During each pulse, it takes 13.8 μs per pixel. So the total excitation time per pixel is 16.56 ms (13.8 μs × 40 × 30). The spatial resolution is 0.2486 × 0.2486 μm per pixel. After photolysis of Diazo-2, Ca^{2+} activities and morphology of the target branch were monitored for 60 min. Embryos loaded with the solvent of Diazo-2 were used as the control.

To induce local Ca^{2+} transients at ETC branches, focal photolysis of NP-EGTA AM/Ca^{2+} complex was conducted as previously described (Ellis-Davies and Kaplan, 1994; Fluck, 1995; Gomez and Spitzer, 1999; Zheng and Poo, 2007). An equal volume of NP-EGTA AM stock solution (16 mM, N6803, Molecular Probes, dissolved in DMSO), and F-127 (20% v/w, P3000, Molecular Probes, dissolved in DMSO) which can facilitate intracellular loading of NP-EGTA AM, were mixed together. The mixture was further mixed with an equal volume of an external solution containing (in mM) 134 NaCl, 2.9 KCl, 2.1 $CaCl_2$, 1.2 $MgCl_2$, 10 HEPES and 10 D-Glucose (pH 7.8, 290 mOsm), to permit NP-EGTA AM to abundantly bind free Ca^{2+}. After centrifugation (9000 × g, 30 min), the supernatant was used as a NP-EGTA working solution (4 mM) in following uncaging experiments. All of the above procedures were performed under the darkness. Before NP-EGTA AM application, spontaneous local Ca^{2+} activities and morphology of ETC branches were monitored for 20 min, and those exhibiting no obvious Ca^{2+} activity and no morphological change were selected for further manipulation. A micropipette (tip diameter, 1 - 2 μm) loaded with the NP-EGTA AM working solution was positioned to the neighboring region of the target ETC from the contralateral optic tectum. The distance between the tip of the micropipette and the apical terminal of the ETC branch was 20 - 30 μm. The NP-EGTA AM working solution was ejected out through gas pressure (3 psi, 50 ms in duration, 1 s in interval, 10 pulses) delivered by a Picospritze III (Parker Picospritzer). Puffing of NP-EGTA was repeated for 3 - 4 times with an interval of 10 min. Then, Ca^{2+} activities and morphology of ETC branches were further monitored to confirm the quiescence of the target ETC branch. For induction of a single Ca^{2+} event, local photolysis of NP-EGTA AM in a ~4 × 4 μm square at the tip region of the target ETC branch was performed with a 405-nm laser at 0.36 mW. The photolysis stimulation lasts 2 s and contains 16 scan pulses (8 pulses per second). During each pulse, it takes 13.8 μs per pixel. So the total excitation time per pixel is 0.22 ms (13.8 μs × 16). The spatial resolution is 0.2486 × 0.2486 μm per pixel. Relative high- and low-frequency local Ca^{2+} transients were induced by repeated the stimulation above with an interval of 2 min and 20 min, respectively. Larvae loaded with the solvent of NP-EGTA AM were used as the control.

Local Puffing and Bath Application of Drugs

Local puffing was performed to locally manipulate Ca^{2+} transients of ETC branches. To suppress Ca^{2+} transients, ETC branches exhibiting not less than 4 Ca^{2+} transients within 20 - 30 min and no obvious morphological change, or no more than 3 Ca^{2+} transients

within 30 min and obvious morphological extension were selected for local puffing of drugs. Local puffing was performed by using a micropipette (tip diameter, 1 - 2 μm) which was introduced from the contralateral optic tectum to the neighboring region of the target ETC branch. Drug solution contained in the micropipette was ejected out by pulses of gas pressure (3 psi, 50 ms in duration, 1 s in interval, 10 pulses). The Ca^{2+} chelator BAPTA AM (15 mM, B1205, Thermo Fisher; dissolved in DMSO) contained in the micropipette was applied when larvae were incubated with a Ca^{2+} free external solution consisting of (in mM) 134 NaCl, 2.9 KCl, 1.2 $MgCl_2$, 10 HEPES and 11.7 D-Glucose (pH 7.8, mOsm 290). The Piezo1 channel blocker GsMTx4 (250 μM, Ab141871, Abcam; dissolved in water) (Bae et al., 2011; Koser et al., 2016; Li et al., 2014) contained in the micropipette was applied when larvae were incubated with the external solution mentioned above. For induction of local Ca^{2+} transients, ETC branches exhibiting no obvious local Ca^{2+} activity and no morphological change were selected for local puffing of the Piezo1 agonist Yoda1 (5586, Tocris; dissolved in DMSO) (Syeda et al., 2015). The working concentration of Yoda1 in the micropipette is 1 mM.

To efficiently block of the activity of Calpain or NOS, bath application of the calpain activity inhibitor Calpeptin (250 μM, C8999, Sigma; dissolved in DMSO) (Tsujinaka et al., 1988) or the NOS inhibitor N^G-Monomethyl-L-arginine (L-NMMA, 500 μM, M7033, Sigma; dissolved in water) (Kashiwagi et al., 2005; Rees et al., 1989) was used. A cut of the skin (~50 μm in the length) between the two mesencephalic veins (MsVs) at the dorsal brain was made with a micropipette. MsVs were kept intact during the entire procedure. After bath application of drugs for 60 min, local Ca^{2+} activities and morphology of ETC branches were monitored for 60 min without washout of drugs. For the co-application of Calpeptin and Yoda1, larvae were first bath incubated in Calpeptin (250 μM)-contained external solution for 1 h, followed by imaging of 20 min, ETC branches exhibiting no local Ca^{2+} transients and no morphological change were then selected for local puffing of Yoda1. Larvae treated with the respective solvent of those drugs were used as the control.

Application of Mechanical Stimuli

To mimic the mechanical stretch on the membrane of ETC branch, pulses of negative pressure via a micropipette attached to the target ETC branch were applied. Larvae were paralyzed with 1 mg/ml α-bungarotoxin (2133, Tocris) and a cut of the skin around the MsVs was made. To avoid the potential involvement of neural activity, tetrodotoxin (TTX, 1 μM, 1078, Tocris) was included in the external solution to block neuronal activity. Before mechanical stretch application, spontaneous Ca^{2+} activities and morphology of ETC branches were monitored for around 20 min, and the ETC branch with no Ca^{2+} transient and no obvious morphological change was selected for further mechanical stretch application. A micropipette (tip diameter, 0.5 - 1 μm) loaded with the dye DiO (5 μM, Vybrant®; dissolved in the external solution), which was used to visualized the tip of the micropipette, was approached to the target ETC branch. After the micropipette tip attached the cell membrane of the target branch at the middle site, 3 pulses of negative pressure (3 psi, 10 s in duration) were applied with an interval of 2 min between pulses. Simultaneously, Ca^{2+} activities and morphological changes of the target branch were imaged. In experiments of Piezo1 blockade, GsMTx4 (5 μM)-contained external solution was bath applied for at least 10 min before mechanical stretch stimulation. To mimic an increase in tissue stiffness near ETC branches, a micropipette with a tip diameter of 5 μm was introduced below the tip of the target ETC branch.

QUANTIFICATION AND STATISTICAL ANALYSIS

The normality of data was first examined with Kolmogorov-Smirnov test. For normally distributed data, the significance of difference between the data obtained from two groups (inter-group, including Figures 1E, 2C, 2D, 2G, 2H, 2L, 2O, 3C–3E, 3H–3J, 4G, 4H, 4K, 4Q, 4T, 4V, 4W, 5B, 5I, S5C, S5E, 6D, 6G, and 6I) or from the same group before and after manipulations (intra-group, including Figures 2C, 2G, 4B, 4G, 4J, 4M, 4P, 4V, 5C, 5F, S5C, and S5E) was determined by using unpaired or paired two-tailed Student's t test, respectively. For non-normally distributed data (including Figures 1D, 4E, 4S, 5H, 6B, 6E, 6H, S3, and S5D), two-tailed Mann-Whitney test or two-tailed Wilcoxon signed rank test was used for inter-group or intra-group data comparison, respectively. For time course analysis of the mean Ca^{2+} transient number in Figure 1E, the p values were obtained by comparing the Ca^{2+} transient numbers at retracting and extending branches at each corresponding time window. For time course analysis of relative length (L/L0) of ETC branches, the p values were obtained by comparing the L/L0 of experiment and control groups at each corresponding time point (unpaired two-tailed Student's t test). Logistic regression and receiver operating characteristic analysis were used for discriminating retraction and extension fates of ETC branches based on frequencies of local Ca^{2+} transients in Figures 1F and S4A, and the boundary frequency of Ca^{2+} transients between branch extension and retraction was calculated as the value at the x axis corresponding to the value of 0.5 at the y axis in the regression curve. Fisher exact test was used in Figure 6C. $p < 0.05$ was considered as statistically significant. Data were represented as mean ± SEM.